Politecnico di Torino

POLITECNICO DI TORINO

Master of Science in Mechanical Engineering

Master of Science Thesis

Analysis of the Thermal-Hydraulic Performance of Gyrotron Cavities Equipped with Mini-Channel Cooling System

Supervisor:
Prof. Laura Savoldi

Co-Supervisor:
Rosa Difonzo

Candidate:
Erdi Uygun
Student ID: S263704

A.Y. 2021/2022

July 2022

Abstract

Mini channel cooling systems have increasing trend of usage in various cooling applications such as computer microprocessors, air conditioning and refrigeration. Depending on the field of interest, geometry and material of mini channel cooling systems vary. On the other hand, mini channel configuration is in the promising direction of effective cooling for high heat load regions as in gyrotron resonance cavity.

In this study, the thermal – hydraulic performance of copper mock-up of an ITER-like (International Thermonuclear Experimental Reactor) gyrotron cavity equipped with semi-circular straight mini channels subjected to inductive heating is studied. The commercial software STAR-CCM+ has been used to develop and simulate 3D – CFD (Computational Fluid Dynamics) model of the entire mock-up.

Firstly, set of numerical results which have been computed in Karlsruhe Institute of Technology – KIT, is used for the calibration of the heating power, the spatial distribution using an electro-magnetic model. Then the calibrated power is used as input to reproduce the steady-state temperature traces when the cavity is cooled using subcooled water.

The results show that, the mini channel configuration provides effective cooling for a region subjected to high heat load for instance 3,5x10^5 W/m^2, and promising results for further studies on this type of configurations.

Keywords: Mini Channel, Heat Exchanger, CFD, Gyrotron Cavity

List of Contents

Abstract ii

List of Figures v

List of Tables viii

Nomenclature ix

Chapter 1 1

1.1 Introduction 1

1.2 Electron Cyclotron Resonance Heating – Gyrotron 2

1.3 Mini Channel Cooling Systems 4

1.4 Commonly Used Software & Programmes 7

1.4.1 Computational Fluid Dynamics 7

1.4.2 Computer Aided Design 7

1.4.3 Data Analysis 8

1.5 Different Cooling Strategies for Gyrotron Cavity 9

1.6 Objectives of the Work 12

Chapter 2 13

2.1 Analysis of Hydraulic Performance of Mini Channels 13

2.1.1 Hydraulic Model 13

2.1.2 Computed results and comparison with experimental results 16

Chapter 3 18

3.1 Description of Work and Experimental Setup 18

3.2 Thermal Model and Comparison to Dry Test Results 22

3.3 Calorimetric Analysis of Tests with Water 29

3.4 Calibration of The Input Power 32

3.5 Validation of The Calibrated Input Power 34

3.6 Analysis of Mock-Up Tests with Water 35

3.6.1 Thermal-hydraulic model 35

3.6.2 Computed results and comparison with experimental results 37

3.7 Conclusions 44

References 46

List of Figures

Figure 1. Structure of the gyrotron with hollow electron beam (yellow) and excited microwave (red) [3]. 3
Figure 2. Variation of heat transfer coefficient with channel size for a square channel under laminar flow, constant heat flux boundary condition, assuming no rarefaction and compressibility effects [4]..... 6
Figure 3. CAD model of the cavity mock-up. Cut of (a) hypervapotron, (b) mini channel, and (c) meander-flow drivers blocks on the symmetry plane [14]. 9
Figure 4. Schematic view of the inner part of the full-size gyrotron cavity (resonator in orange) in a stainless-steel envelope, for the European 170-GHz, 1-MW gyrotron for ITER. The inner diameter of the cavity is approx.2 cm [15]. 10
Figure 5. CAD sections of the mock-up equipped with mini-channels (a) and with Raschig rings (b) [16]. 11
Figure 6. Section of the geometry used for the mock-up thermal model. The gray solids refer to stainless-steel, the pink parts to Glidcop. In the insert: azimuthal distribution of the load on the cavity surface, as from the EM simulations with 1800 W of inductor power [17]..... 11
Figure 7. a) Section of mock-up used in hydraulic model, grey colour refers to stainless steel and red to copper. 1 – Resonator, 2- Water Stopper, 3 – Front Insert, 4 – Back Insert, 5 – Fluid Discharger, 6 – Fluid inlet tube, 7 – Fluid outlet tube. b) Zoom-in mini channels 13
Figure 8. Sketch of the reference geometry for the full hydraulic simulations, also including the water domain (in blue). Half of the computational domain is shown. 14
Figure 9. Computational fluid domain of entire mock-up. 15
Figure 10. Experimental and computed pressure drop comparison for different flow rates. .. 17
Figure 11.. Section of mock-up used in thermal model, grey color refers to stainless steel and red to copper. 1 – Mantel, in Austenitic Stainless Steel, 2- Front insert, in Austenitic Stainless Steel, 3 – Back Insert, in Austenitic Stainless Steel, 4 – Water stopper 18
Figure 12. Block diagram of the experimental set-up: mini channel cooling mock-up, thermocouples (TC1…TC16), PT100 thermometers (PT100 1 – PT100 4), pressure sensors, flow meter, MINAC6 inductor heater with hand- held transformer and the inductor head, as well as S7–300® hardware and a computer with WIN CC® software [17]..... 19

Figure 13. Complete experimental set-up: mini-channel cooling mockup, thermal sensors, pressure sensors and the inductor heating coil [17]. 20
Figure 14. Elements of experimental hardware: a) Inductor heating coil, b) pressure sensor, c) flow meter, d) PT100 resistivity thermometer and e) thermocouple type K [17]..... 20
Figure 15. Model for EM simulations: mini-channel mock-up with inserted inductor heater head [17]. 22
Figure 16. a) Polyhedral mesh on a longitudinal section of the upper half of the solid parts for the pure thermal model of the mock-up, and b) zoomed view on the transversal section highlighted in (a). 22
Figure 17. Zoom-in transversal section across two thermocouples located at different depths with respect to inner wall of resonator. 23
Figure 18. Setup of the thermal simulations: adiabatic boundary conditions are applied everywhere, except in the inner surface of the cavity, where the applied heat load peak is highlighted in red 24
Figure 19. (a) Temperature dependence of copper conductivity λ and (b) specific heat cp and density ρ, as adopted in the numerical simulations. 24
Figure 20. (a) Temperature dependence of stainless-steel conductivity λ and (b) specific heat cp and density ρ, as adopted in the numerical simulations. 25
Figure 21. Longitudinal distribution of the heat flux computed by the EM simulations with Q_IH = 1800 W. The values at the same z refer to different azimuthal location around the heated surface. 26
Figure 22. Temperature evolutions of TCs for a) Q_IH = 600 W b) Q_IH = 1200W c) Q_IH = 1800 W. Blue lines indicate simulation results, red lines the experimental results for all figures. 27
Figure 23. Thermocouple temperature comparison in the dry conditions, at 600s for Q_IH =1800. Blue bars indicate simulation results, red bars the experimental results. In the inset, the radial position of the Tc is reported. 28
Figure 24. Calorimetric power evolution at 1800 W inductive power for 10 l/min flow rate. 30
Figure 25. Calorimetric power at different water flow values with its error bar, compared to the integral power from EM model (stars). 31
Figure 26. Average calorimetric power in comparison with EM mode and compared to the integral values of the calibrated heat load obtained in 2020 [17] work. 32

Figure 27. (a) Parabolic fit for the Q_EM multiplier at different Q_IH (open circle: calorimetry data, open triangles: extrapolated data) (b) Spatial distribution of the calibrated heat load for Q_IH = 1800 W. 33
Figure 28. Thermocouple temperature comparison at 600s for Q_IH =1800. Blue bars indicate simulation results, red bars the experimental results. 34
Figure 29. Sketch of the reference geometry for the full 3D thermal-hydraulic simulations, also including the water domain (in blue). Half of the computational domain is shown. The heat load peak is applied in the red region. 35
Figure 30. Polyhedral mesh of the a) longitudinal section of the solid and fluid part, and b) zoomed in view of the channel outlet region. 36
Figure 31. a) Highlighted: Transverse section across the mock-up where TCs 2,3,6,7,10,11,14 and 15 are located, b) Temperature map computed across the section in (a), also showing the TC location.....37
Figure 32. Test with water 20 l/min and QIH = 1800 W: comparison of experimental and computed TC temperature increases at steady state. 38
Figure 33. Test with water 20 l/min and QIH = 2400 W: comparison of experimental and computed TC temperature increases at steady state 38
Figure 34. Test with water 20 l/min and QIH = 3000 W: comparison of experimental and computed TC temperature increases at steady state. 39
Figure 35. Comparison between current experiments and 2020 ones [12] for 20 l/min of flow rate and 2400 W of inductive power. Measured and computed temperature differences are represented. 40
Figure 36. Relative errors evaluated with respect to the measured temperature differences for all TCs in 1800, 2400 and 3000W. 41
Figure 37. Temperature differences with (a) R_th=1×10^(-5) (m^2 K)/W and (b) with R_th=5×10^(-5) (m^2 K)/W for 2400 W compared to null R_th and experimental results...42
Figure 38. Relative errors evaluated with respect to the measured temperature differences for all TCs with different values of R_th for 2400 W. 43

List of Tables

Table 1. Experimental results of pressure drop (with uncertainties) of the mock-up for different flow rates. 15
Table 2. Comparison of experimental and computed pressure drop values for different flow rates. 16
Table 3. Integral value of the heat load on the inner wall as computed by the EM model, at different power level of the IH 26
Table 4. Input measured data for the calorimetric evaluation of the power, and measured water inlet pressure 29
Table 5. Calorimetric Power with Uncertainties at different nominal power levels in comparison with Integral Powers from EM model and simulation. 31
Table 6. IH Nominal power, EM Model power and Calibrated Power according to the computed parabolic fit. The 2020 calibration results are also reported for the sake of comparison. 33

Nomenclature

ITER	International Thermonuclear Experimental Reactor
ICRH	Cyclotron Resonance Heating
ERCH	Electron Cyclotron Resonance Heating
MC	Mini channels
Dh	Hydraulic diameter
IC	Integrated circuit
CFD	Computational Fluid Dynamics
HPC	High-Performance Computing
CAD	Computer Aided Design
KIT	Karlsruhe Institute of Technology
EM	Electro-magnetic
IH	Inductive heater
Q_cal	Deposited power computed by calorimetry
Q_EM	Deposited power computed using the EM model
Q_IH	Input power of the IH
T	Temperature
TC	Thermocouple
λ	Thermal conductivity [W/mK]
cp	Specific heat [J/kgK]
ρ	density [kg/m^3]
m	mass flow rate [kg/s]

Chapter 1

1.1 Introduction

Nowadays, the carbon emission reduction and hence aiming the zero-carbon release due to fossil fuel usage especially in electricity production is one of the main focal points of the countries. Main idea behind these actions is the effects of global warming – climate change which are evidently experienced in daily life not only in experiments and negative effects of fossil fuel-based products, such as increased pollution in oceans. In this transition phase, nuclear fusion plays an important role being candidate for non-carbon emitting and so-called limitless energy as our Sun and stars.

International Thermonuclear Experimental Reactor – ITER organisation has been established for this purpose in 2007 [1] with collaboration of 35 nations to build the world's largest Tokamak which is a magnetic fusion device. One of the conditions to achieve fusion in a laboratory is the temperature which is on the order of 150 million degrees Celsius. Tokamak will be using three different sources of heating which are Neutral Beam Injection, Ion Cyclotron Resonance Heating (ICRH) and Electron Cyclotron Resonance Heating (ERCH).

Electron cyclotron heating method uses radio waves at different frequencies, specifically 1-MW Gyrotron operating at 170 GHz with a pulse duration of more than 500s. The advantage of the ERCH is that the beam can be transmitted through air which simplifies the design and allows the source to be far from the plasma, simplifying maintenance [2].

The resonator part of the gyrotron so-called "cavity" is subjected to high heat where the rotational kinetic energy of electrons is converted into microwave energy. This resonant cavity needs an effective cooling in order to sustain a reliable operation. For this purpose, in the past, different cooling strategies were tested, and it turns out that the mini channel cooling system configuration is one of the most promising designs for the gyrotron cavity.

1.2 Electron Cyclotron Resonance Heating – Gyrotron

Gyrotrons are powerful microwave sources, i.e., they emit electromagnetic waves at very high frequency and intensity. This gyrotron frequency corresponds to a wavelength of approx. 3 mm. When the heating microwave frequency equal to the electron rotation frequency in the magnetic field confining the plasma, or to its harmonics is named as Electron Cyclotron Resonance Heating (ERCH).

The main parts of a gyrotron are an electron gun, an acceleration chamber, a resonance chamber (cavity) immersed in a strong magnetic field, a mode converter and finally of a collector of electrons, all of which are placed inside a vacuum tube [3].

The electron gun produces a hollow beam of electrons, which rotate in a strong magnetic field. This beam is accelerated and changed in form by a changing electric and magnetic field. Inside the superconducting magnets, where the magnetic field is strongest, the relativistic electrons enter the resonance chamber (cavity). Because their rotational motion is the same as the resonance frequency of the cavity, they can interact with the electromagnetic wave inside the cavity. The rotating electric field of the wave decelerates the rotational motion of (most of) the electrons, so that the electrons give rotational energy to the wave. By this mechanism, the microwave is created inside the cavity [3].

The hollow electron beams leave the cavity in line with the microwave radiation. This radiation is transformed into another field profile (mode) in the mode converter and is directed via several mirrors to a window, where the radiation exits the gyrotron. The electron beam, which has given part of its energy to the microwave, continues in the same direction and is directed against the wall of the collector. This way, the remaining energy of the beam heats the collector wall, which makes an effective cooling of the collector necessary [3].

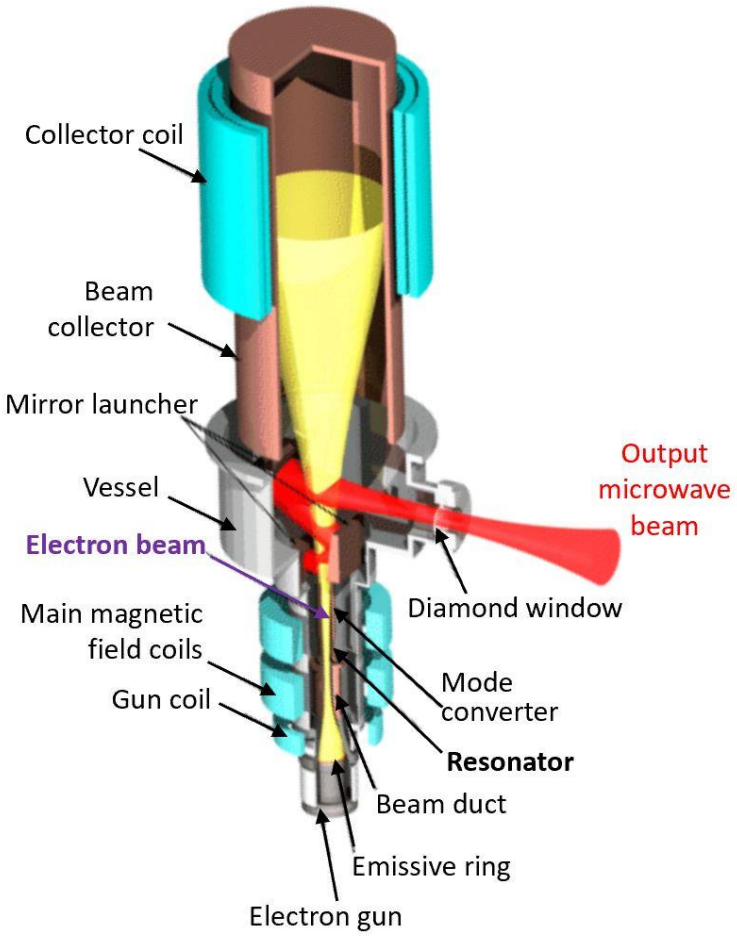

Figure 1. Structure of the gyrotron with hollow electron beam (yellow) and excited microwave (red) [3].

1.3 Mini Channel Cooling Systems

It is always possible to observe the nature to try and find an answer to a problem mimicking its behaviour, shape, physics, etc. This could be flap of a bird, shape of a water droplet or heart of a human as volumetric machine. We could say that the small channels have important role in biological systems as in veins. Fluid flow and mass transfer in human body are supplied thanks to mini and micro channels. By following the nature's footsteps, mini and micro channel configurations are widely utilized for cooling microprocessors or lasers for high heat loads.

Mini channel configurations are becoming more popular as components in heat exchangers. These heat exchangers are used in various industrial applications with many different geometries and lengths. The ability to produce tubes with external or internal fins and with smaller wall thicknesses allows higher heat transfer area per unit volume of a tube. Therefore, mini channel tubes are ideal for use in compact and light weight heat exchangers.

The classification scheme based on the hydraulic diameter – Dh for microchannels, mini channels, and conventional channels is proposed as follows which is recommended for single-phase as well as two-phase applications [4].

Conventional Channels:	Dh >3 mm
Mini channels:	3 mm ≥ Dh > 200 μm
Microchannels:	200 μm ≥ Dh > 10 μm
Transitional Channels:	10 μm ≥ Dh > 0.1 μm
Transitional Microchannels:	10 μm ≥ Dh > 1 μm
Transitional Nanochannels:	1 μm ≥ Dh > 0.1 μm
Molecular Nanochannels:	0.1 μm ≥ Dh

Conventional techniques are applied in making the channels of 3 mm or larger hydraulic diameter. The channel sizes below about 3 mm are formed as narrow fin passages, as in plate-fin heat exchangers. The regenerative heat exchanger matrix and plate heat exchangers belong to this category. The lower limit for manufacturing smaller channels is really imposed by the major changes in fabrication technology warranted below about μm 200 m. The range for

compact heat exchanger passages is expected to decrease in the future, with the hydraulic diameter range 200 μm to 3 mm classified as compact heat exchangers [4].

Heat transfer enhancement in mini channels could be achieved by secondary fins on the surface – micro fins, different channel geometries, and rough surfaced. Employment of sharp corners for efficient liquid drainage in condensing application provide heat transfer augmentation [5].

Owing to their higher thermal performance, mini channels are being increasingly employed in process applications; the higher pumping power requirements are offset with the overall size and cost reductions. In the automotive and aero industry, mini channels proved to be valuable in addressing the severe space constraints. Compact heat exchangers employ mini channels in these and many other applications. The microelectronics engineers, conversant with the submicron scale in their IC designs, and the mechanical engineers, familiar with the mini channels in compact heat exchangers, found the microchannel range as a desirable compromise in microelectronics cooling application. In biomedical and optical applications, transitional nanochannels are often employed. The race is far from over, mechanical engineers moving from the comfortable confines of heat sinks mounted on electronics devices, components, and assemblies, to the uncharted territories of microchannels, partnering with the microelectronics engineers for their on-chip flight to meet the new micron and sub-micron sized thermal and fabrication challenges. Understanding of these systems will enable us to proceed to the next level of nanochannels in biological applications [4].

A typical mini channel heat exchanger employs a flat tube with triangular or rectangular passages of 1–2.5 mm hydraulic diameter. Still smaller passages are being applied in condenser applications, 25-mm or wider, and length dependent on the refrigerant and operating conditions [6].

In addition to the heat transfer considerations, pressure drop penalty also needs to be carefully evaluated when selecting the channel size. The pressure gradient (pressure drop per unit length) increases drastically with channel size reduction, but it was also noted that mini channel heat exchangers need to be suitably designed to provide short flow lengths to limit the overall pressure drop [7] Today's compact heat exchangers are successfully implemented in various applications, and higher-pressure gradients in mini channel heat exchangers simply become a design constraint in arriving at a suitable heat exchanger design [6].

The effect of hydraulic diameter on heat transfer and pressure drop is illustrated in Fig.1 for water and air flowing in a square channel under a constant heat flux and fully developed laminar flow conditions. The heat transfer coefficient is unaffected by the flow Reynolds number in the fully developed laminar region [4].

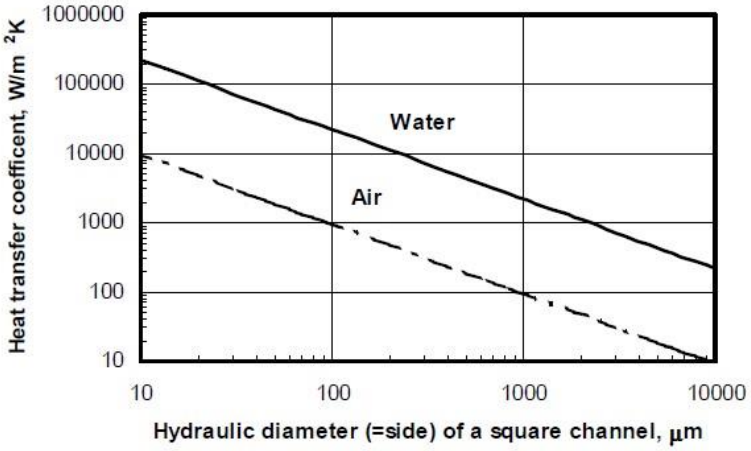

Figure 2. Variation of heat transfer coefficient with channel size for a square channel under laminar flow, constant heat flux boundary condition, assuming no rarefaction and compressibility effects [4].

1.4 Commonly Used Software & Programmes

1.4.1 Computational Fluid Dynamics

Computational fluid dynamics (CFD) is considered nowadays a powerful tool in the field of fluid flow problem solving. This method is based on the numerical solution of fluid flow equations with a discretization of the spatial domain. The most common approach to CFD analysis is the finite volume method: this method consists in the domain discretization into a finite set of control volumes where general conservation (transport) equations for mass, momentum, energy, species, etc. are solved. Partial differential equations are thus discretized into a system of algebraic equations solved numerically to obtain the global solution [8].

Comparing the available commercial softwares, Siemens Star CCM+ is selected to be used for meshing and simulations. On the other hand, mimicking the real-world scenarios, mainly experiments, requires high computational cost for workstations. Taking into account these limitations, we acknowledge that simulations have been run on the High-Performance Computing – HPC units by courtesy of Department of Control and Computer Engineering at Politecnico di Torino [9].

Simcenter STAR-CCM+ is a multiphysics computational fluid dynamics (CFD) software for the simulation of products operating under real-world conditions. Simcenter STAR-CCM+ uniquely brings automated design exploration and optimization to the CFD simulation toolkit. The single integrated environment includes everything from CAD, automated meshing, Multiphysics CFD, sophisticated postprocessing, and design exploration. This allows engineers to efficiently explore the entire design space to make better design decisions faster [10].

1.4.2 Computer Aided Design

CAD, or computer-aided design and drafting (CADD), is technology for design and technical documentation, which replaces manual drafting with an automated process. If you're a designer, drafter, architect, or engineer, you've probably used 2D or 3D CAD programs [11].

SOLIDWORKS® has been the trusted industry standard in design and engineering. Intuitive 3D design and product development solutions from SOLIDWORKS help conceptualize, create, validate, communicate, manage, and transform the innovate ideas into great product designs [12]. Considering the benefits of creating 3D models and 2D drawings of complex parts and

assemblies also compatible file extensions which is important for import geometries in simulation software, in this case Star CCM+, made SOLIDWORKS the best solution for CAD design.

1.4.3 Data Analysis

Important parts of the technical reports are how you interpret, process, and present the data. This is why it is important to use a proper software to handle these issues properly. Considering the wide spectrum of working field and ease of use, MATLAB was the choice for data analysis.

MATLAB provides; datatypes and pre-processing capabilities designed for engineering and scientific data, interactive and highly customizable data visualizations, apps and live editor tasks that helps with interactive data cleaning, preparation, and code generation, thousands of prebuilt functions for statistical analysis, machine learning, and signal processing, extensive and professionally written documentation, accelerated performance with simple code changes and additional hardware, expanded analysis to big data without big code changes, automatic packaging of analysis into freely distributable software components or embeddable source code without manually recoding algorithms, sharable reports automatically generated from your analysis [13].

1.5 Different Cooling Strategies for Gyrotron Cavity

In this section, different cooling strategies for gyrotron cavity cooling will be investigated in order to provide a better understanding for this study.

Firstly, three different pressurized subcooled water-cooling options [hypervapotron, mini-channels (MCs), and meander flow drivers] for a full-size gyrotron cavity are developed and analyzed using the commercial computational fluid dynamics code STAR-CCM+. The conjugate multiphase heat transfer problem is solved in the three mock-up geometries, aimed at comparatively assessing their thermal performance at increasing heat load on the target up to 24 MW/m2. The most promising option for an effective cooling of the cavity results to be the mini channels [14].

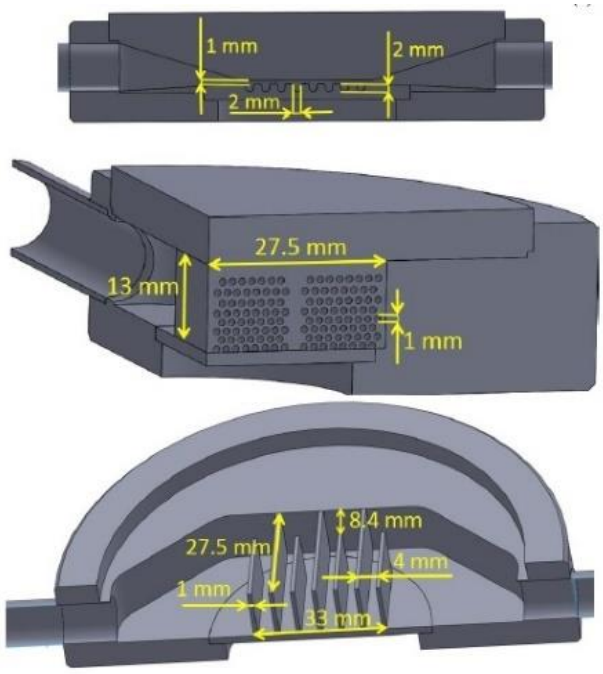

Figure 3. CAD model of the cavity mock-up. Cut of (a) hypervapotron, (b) mini channel, and (c) meander-flow drivers blocks on the symmetry plane [14].

Following the above-mentioned study, another study aiming the characterization of the cooling capacity of the cavity is proposed. A Glidcop target is heated with an electron beam gun with resulting peak heat fluxes relevant for the full-size cavity. Underneath the target surface, whose

temperature is monitored by means of a pyrometer, a set of parallel semi-circular mini channels, with a diameter of 1.5 mm, allow the flow of pressurized water, entering the mock-up at 9 bar and 40 °C. The experimental results show that the mock-up is capable to withstand heat fluxes of 21 MW/m2, while the cooling system keeps the heated surface below 400 °C, for flow conditions comparable to those of the full-size cavity. In view of its reliability, this model might eventually be a useful tool for the simulation of the full-size gyrotron cavity operation [15].

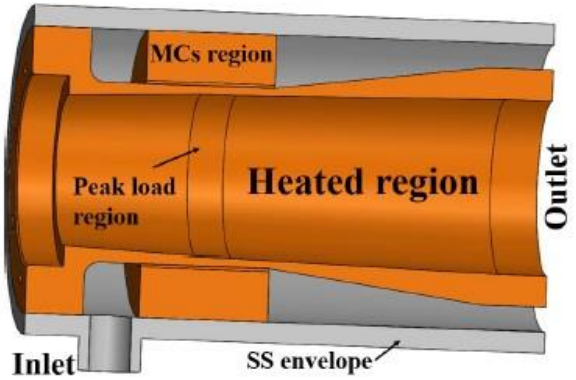

Figure 4. Schematic view of the inner part of the full-size gyrotron cavity (resonator in orange) in a stainless-steel envelope, for the European 170-GHz, 1-MW gyrotron for ITER. The inner diameter of the cavity is approx.2 cm [15].

In a recent study, the design and manufacturing of different full-size mock-ups of the resonance cavity of gyrotrons, relevant for fusion applications, were performed according to two different cooling strategies. The first one relies on mini channels, which are very promising in the direction of increasing the heat transfer in the heavily loaded cavity, but which could face an excessively large pressure drop, while the second one adopts the solution of Raschig rings, already successfully used in European operating gyrotrons. When the validated models were used to compare the two optimized cooling configurations, it resulted that, for the same water flow, the mini-channel strategy gave a pressure drop was two-fold greater than that of the Raschig rings strategy, allowing a maximum flow rate of 1x10^3 m3/s to meet a maximum allowable pressure drop of 0.5 MPa [16].

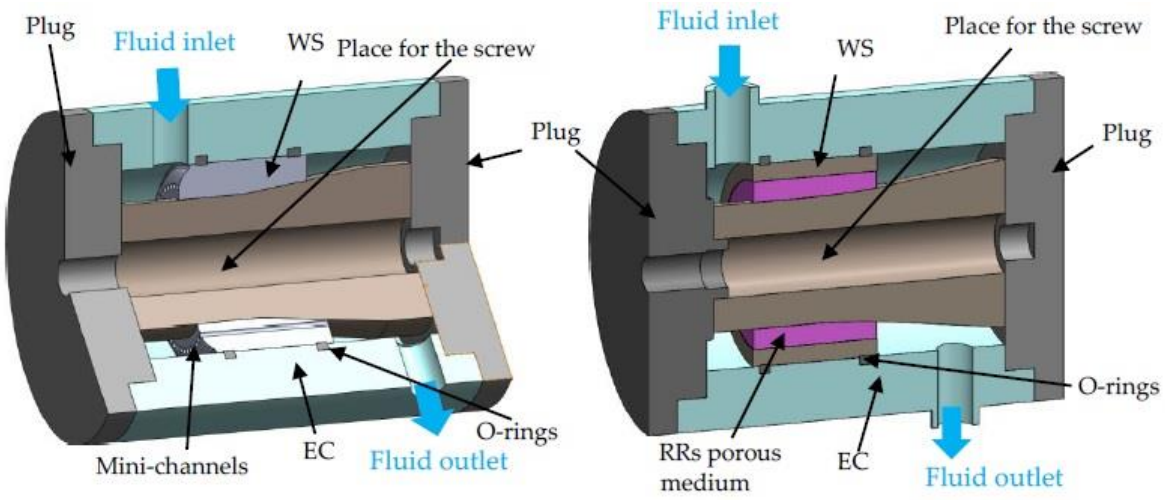

Figure 5. CAD sections of the mock-up equipped with mini-channels (a) and with Raschig rings (b) [16].

In the collaborative work between Karlsruhe Institute of Technology (KIT) and Politecnico di Torino, the experimental investigation of a mini-channel cavity cooling using a mock-up test set-up is described [17]. The mock-up test set-up will be used to experimentally validate the predictive simulation results and verify the mini-channel cooling performance. Calorimetry measurements are performed, and the experimental results are compared with the simulation results obtained with a 3D thermal-hydraulic model, using the commercial software STAR-CCM+. When the calibration factor is applied, the experimental calorimetry is well reproduced by the simulations [17]. The results of experimental study have proved the efficiency of mini channel cooling.

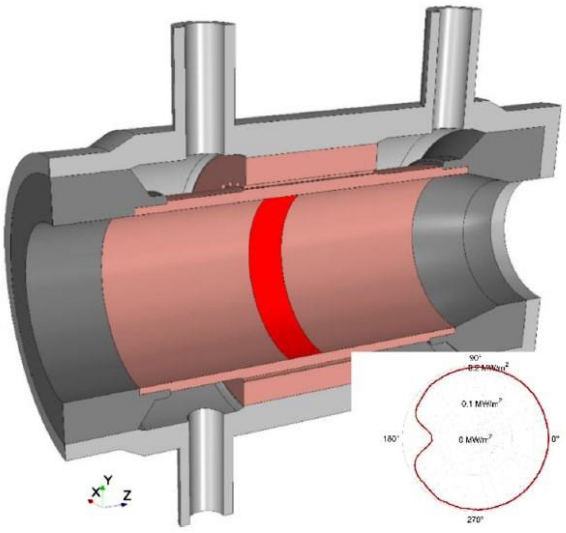

Figure 6. Section of the geometry used for the mock-up thermal model. The gray solids refer to stainless-steel, the pink parts to Glidcop. In the insert: azimuthal distribution of the load on the cavity surface, as from the EM simulations with 1800 W of inductor power [17].

1.6 Objectives of the Work

The present work has the double aims of validate the thermal-hydraulic model used for the study of the mini channels (MC) cooling system of the Gyrotron resonant cavities and investigate the performances of the MC system. The hydraulic performance of the mini channel configuration is validated by comparing the experimental results of a mock-up realized at THALES [18] with numerical simulations. To validate the thermal-hydraulic performance, a mock-up of the cavity equipped with mini channels has been manufactured at Karlsruhe Institute of Technology (KIT) with same design of the one described in [17] but using copper as material of the cavity instead of Glidcop, as in [17]. The mock-up has been realized with traditional machining techniques and tested.

A numerical CFD model of the mock-up has been developed issuing the commercial computational software STAR-CCM+ [19]. The work is articulated in several steps and analysis:

- Comparison of the hydraulic results of the numerical model of the mock-up, based on the experiments performed at THALES [https://www.thalesgroup.com/en].
- Comparison of the numerical results of the numerical (thermal) model of the mock up, based on an electromagnetic (EM) model of the inductive heater (IH) with the experimental results coming from a first test campaign without active cooling (“dry” tests).
- Calorimetric analysis of test results from a second test campaign with water as coolant and calibration of the heat flux deposited into the sample
- Comparison of the numerical results of the CFD model of the mock up, based on the calibrated model of the inductive heating, with the experimental results coming the second test campaign with water as coolant and calibrated heat flux deposited into the sample (steady state)

Chapter 2

2.1 Analysis of Hydraulic Performance of Mini Channels

2.1.1 Hydraulic Model

The mock-up is realized by additive manufacturing rather than conventional techniques at THALES in order to take advantage of ability to create complex geometries for future applications and enhance the heat transfer thanks to surface roughness which could be problematic for other applications. Unfortunately, due to unexpected events, thermal experiments could not be performed and hence, only hydraulic performance of this mock-up is evaluated. The mock-up is composed of six different parts with two different materials which can be seen in Figure 7-a. There are 70 mini channels located on the perimeter of the resonator, having the maximum height of 1.25 mm which varies along the channel. Fluid flow is supplied through an inlet pipe (see Figure 7-a).

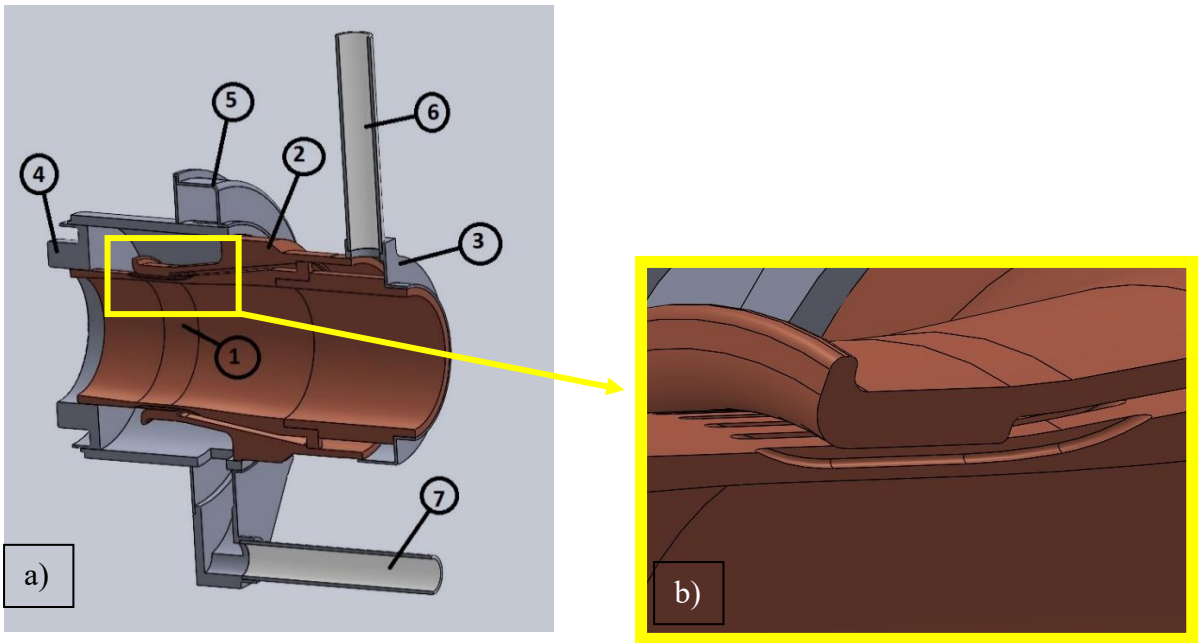

Figure 7. a) Section of mock-up used in hydraulic model, grey colour refers to stainless steel and red to copper. 1 – Resonator, 2- Water Stopper, 3 – Front Insert, 4 – Back Insert, 5 – Fluid Discharger, 6 – Fluid inlet tube, 7 – Fluid outlet tube. b) Zoom-in mini channels

A pure hydraulic model of the entire mock-up has been developed using the commercial software STAR-CCM+ [19], in order to validate its hydraulic performance versus experiments. For the computational grid, a polyhedral mesh with base size of 0.75 mm has been used. It is refined for the mini channel region with base size of 0.1 mm. A total number 22 M cells is obtained. Since this analysis covers only hydraulic evaluation, only fluid domain is considered.

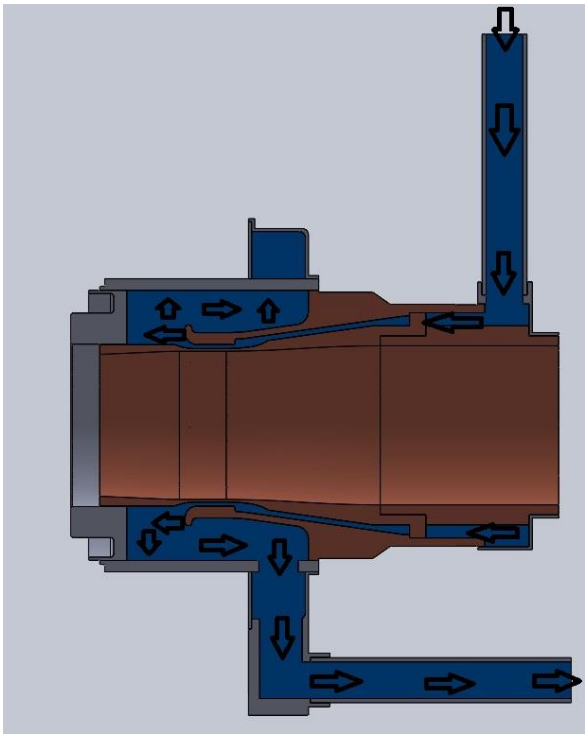

Figure 8. Sketch of the reference geometry for the full hydraulic simulations, also including the water domain (in blue). Half of the computational domain is shown.

The 3D steady-state conjugate thermal-hydraulic model has been then developed for the entire mock-up using the commercial software STAR-CCM+.

The k-ε Lag EB turbulence model, with all y^+ wall treatment, is adopted in the simulations since it can capture the flow detachment downstream of the mini-channels region. This turbulence model has been already demonstrated to be the best, among advanced k-ε and k-ω models, for the simulation of the hydraulic performance of mini channels [20].

The mesh built in the fluid domain account for 22M cells (Figure 8). The base size is defined as 0.75 mm then refined in channels, upstream and downstream of mini channels as 0.1 mm and 0.35 mm, respectively. The thickness of the first wall prism layer has been defined in order

to obtain a dimensionless wall distance $y^+ \sim 1$. The hydraulic analysis is performed in steady state using a segregated solver.

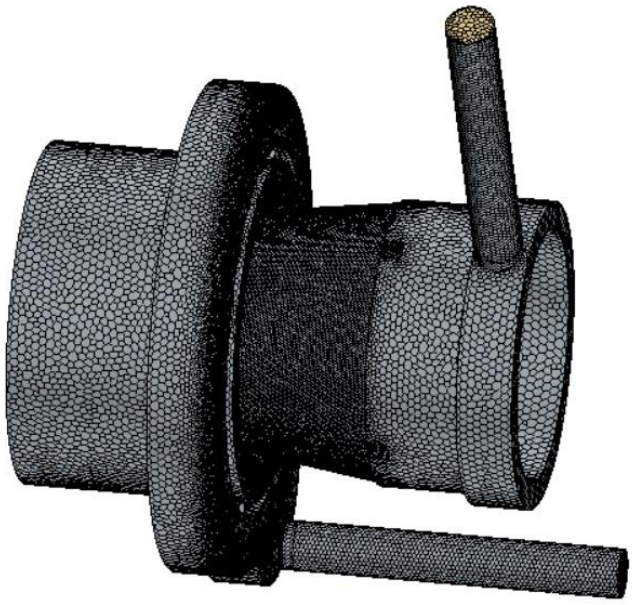

Figure 9. Computational fluid domain of entire mock-up.

The pressure drop of the entire mock-up has been evaluated for 8 different flow rates, starting from 10 l/min to 80 l/min, see the Table 1. Note that only the dataset at the highest flow rate could be used with the adopted turbulence model, since the lowest flow rate value would result in the transition regime.

Table 1. Experimental results of pressure drop (with uncertainties) of the mock-up for different flow rates.

Flow Rate [l/min]	**Pressure drop ΔP [bar]**
10	0.1 ± 0.2
20	0.2 ± 0.2
30	0.5 ± 0.2
40	0.9 ± 0.2
50	1.2 ± 0.2
60	1.9 ± 0.2
70	2.4 ± 0.2
80	2.8 ± 0.2

2.1.2 Computed results and comparison with experimental results

The steady-state simulations have been run for 8 different flow rates and pressure drop values are compared to experimental results in Table 2.

Table 2. Comparison of experimental and computed pressure drop values for different flow rates.

Flow Rate [l/min]	Experimental Pressure Drop [bar]	Computed Pressure Drop [bar]
10	0.1 ± 0.2	0.1
20	0.2 ± 0.2	0.2
30	0.5 ± 0.2	0.5
40	0.9 ± 0.2	0.8
50	1.2 ± 0.2	1.3
60	1.9 ± 0.2	1.8
70	2.4 ± 0.2	2.4
80	2.8 ± 0.2	3.1

For all the flow rates, except 80 l/min, the computed results show a good agreement with experimental results, see the Figure 10. Especially for flow rates 10, 20, 30 and 70 l/min, the computed results provide exact match with experimental values. On the one hand, for flow rates 40, 50 and 60 l/min the computed values stay within the uncertainty limits of experimental values. On the other hand, for the flow rate of 80 l/min, there is an overestimation for the computed value. This could be explained by numerical error of the computer and/or turbulence model which in this case does not seem like a good explanation since other computed results do not show discrepancies. Another explanation could be experimental underestimation due to a common issue of closed circuits/loops, the leakage which could not be fully compensated for especially high flow rates.

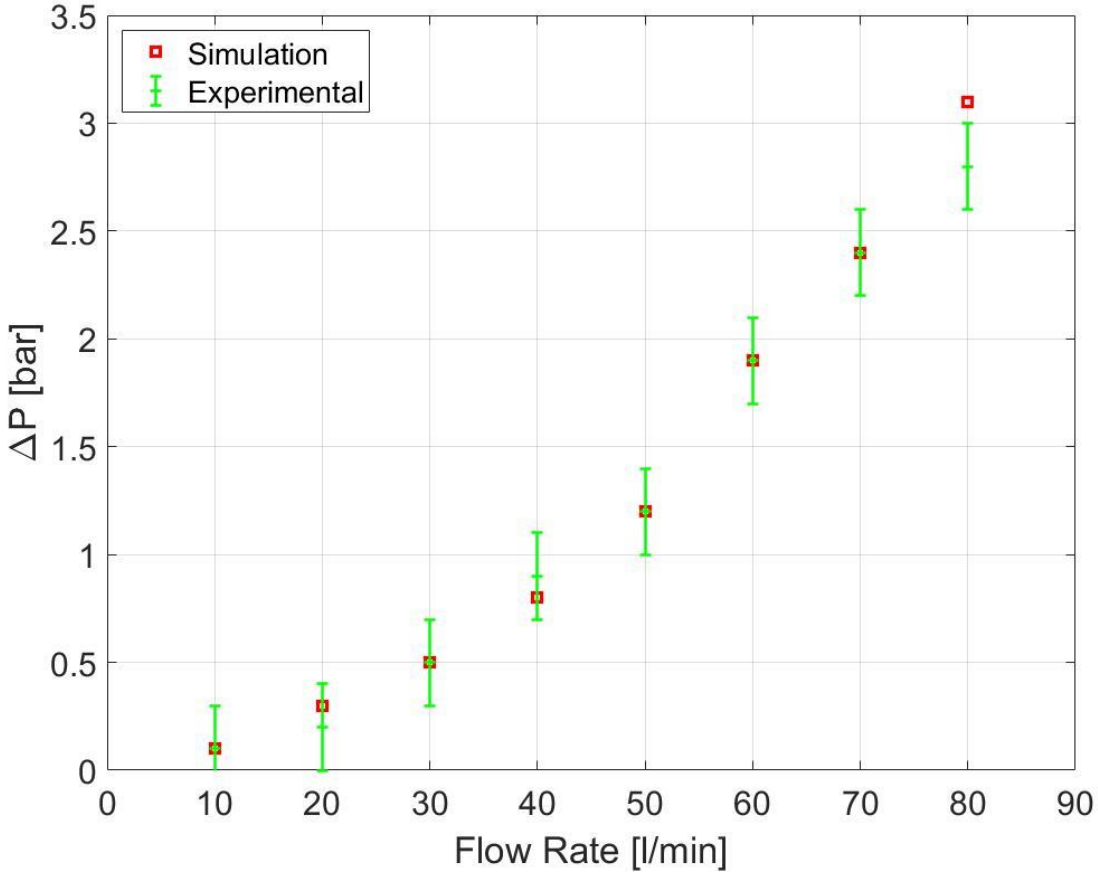

Figure 10. Experimental and computed pressure drop comparison for different flow rates.

In Figure 10, it can be seen that the numerical and experimental results show very good agreement. This is quite promising result for mini channel configuration since the pressure drop has been considered as an issue due to decreased channel size at heat transfer region.

Chapter 3

3.1 Description of Work and Experimental Setup

The mock-up is composed of five different parts with two different materials which can be seen in Figure 4. The water stopper part is located at the middle of the resonator body which has 40 mini channels in half-cylinder shape having 2.8 mm diameter. Coolant flow is supplied through two inlet pipes and two pipes for the outlet in parallel.

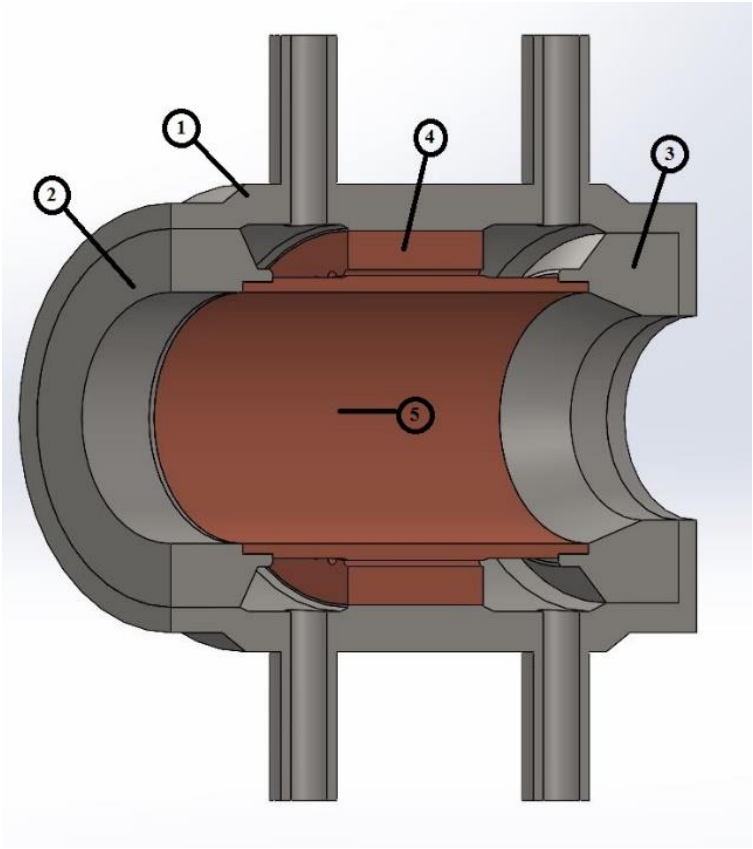

Figure 11.. Section of mock-up used in thermal model, grey color refers to stainless steel and red to copper. 1 – Mantel, in Austenitic Stainless Steel, 2- Front insert, in Austenitic Stainless Steel, 3 – Back Insert, in Austenitic Stainless Steel, 4 – Water stopper

The mock-up is equipped with 16 thermocouples (TC) around the resonator at different depths with respect to the inner wall of the resonator and one temperature sensor at each one of the two inlets and outlets.

The induction heater (MINAC 6®, EFD Induction) induces, at the power level of 3000 W, the thermal loads up to ~1.2 MW/m2 on the cavity inner wall. Acquisition sub-system is implemented in the cavity cooling test system for visualization and recording of the measured values [17].

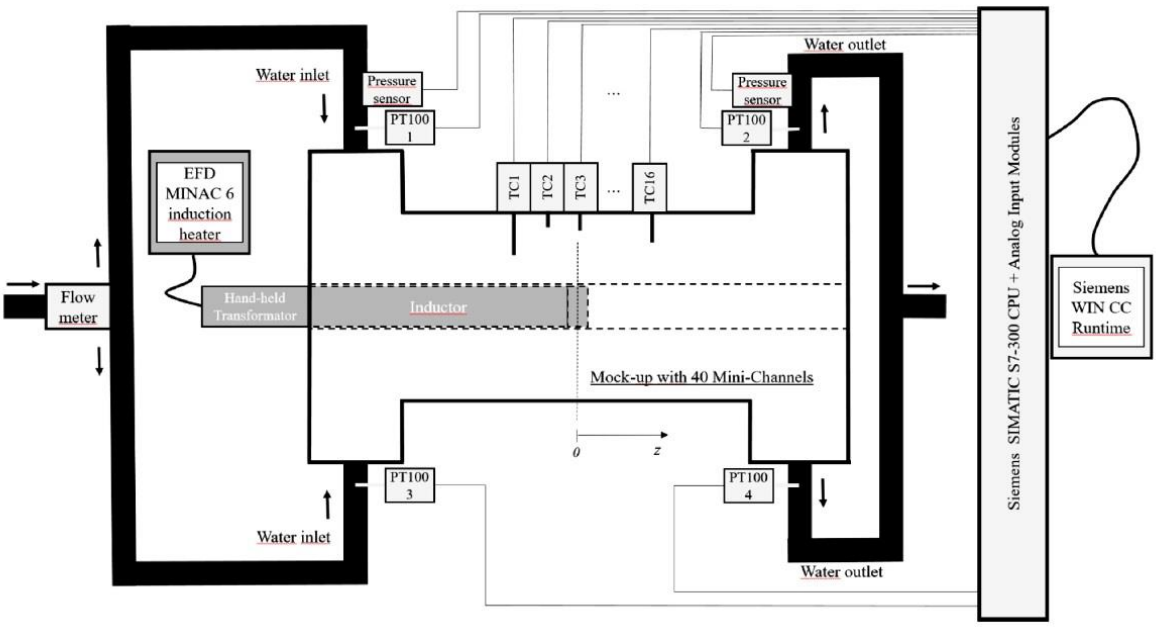

Figure 12. Block diagram of the experimental set-up: mini channel cooling mock-up, thermocouples (TC1…TC16), PT100 thermometers (PT100 1 – PT100 4), pressure sensors, flow meter, MINAC6 inductor heater with hand- held transformer and the inductor head, as well as S7–300® hardware and a computer with WIN CC® software [17].

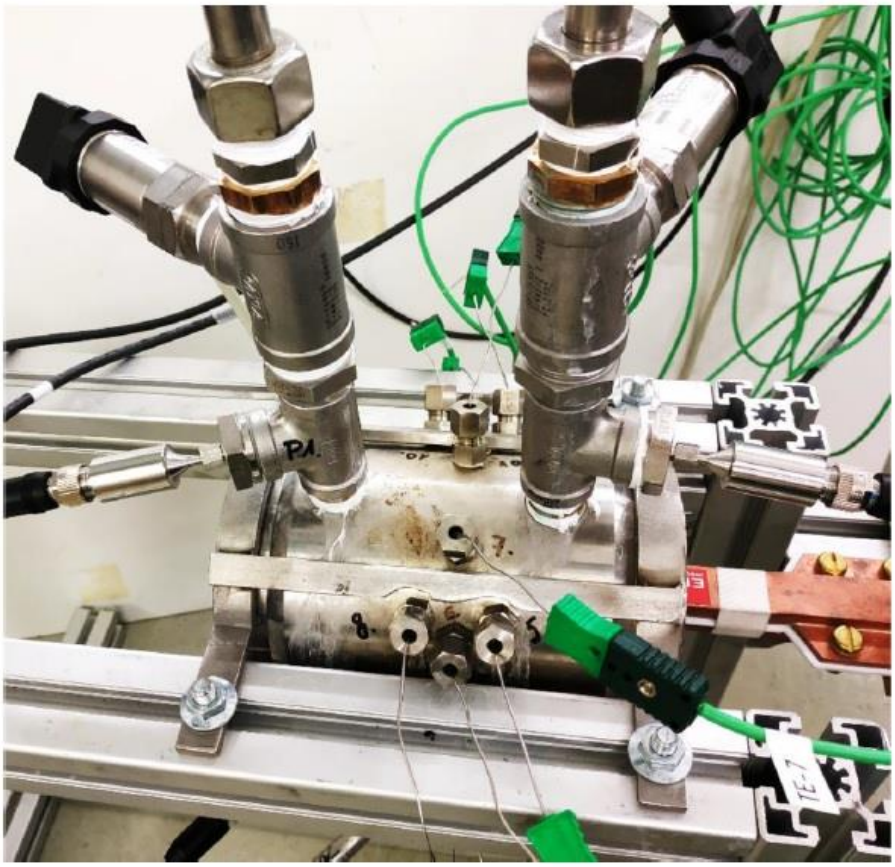

Figure 13. Complete experimental set-up: mini-channel cooling mockup, thermal sensors, pressure sensors and the inductor heating coil [17].

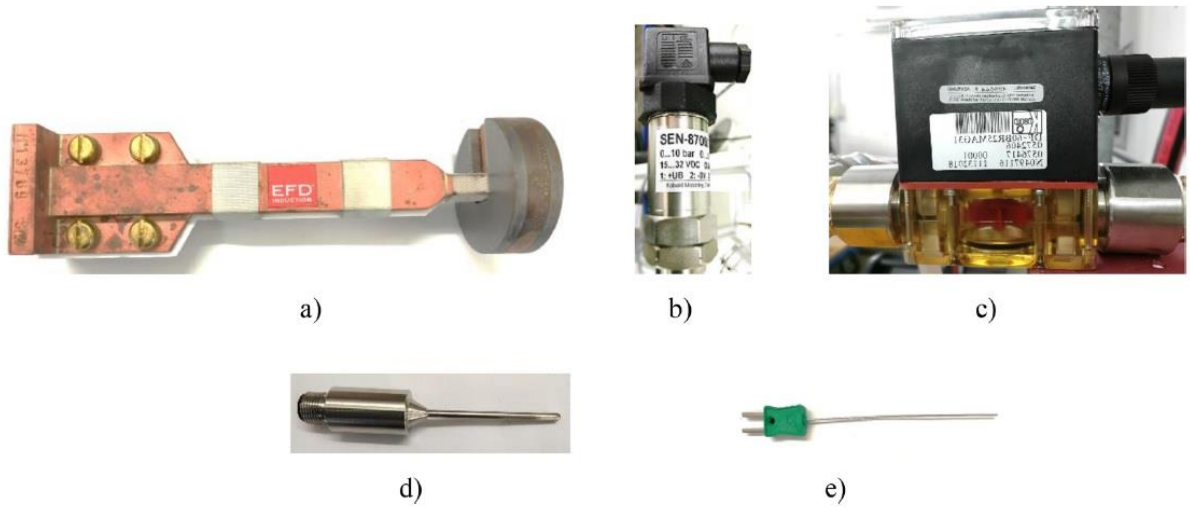

Figure 14. Elements of experimental hardware: a) Inductor heating coil, b) pressure sensor, c) flow meter, d) PT100 resistivity thermometer and e) thermocouple type K [17].

Described induction heater provides a well-defined localized, controllable, and reliable heating. It is also advantageous for experimental validation of 3D thermal-hydraulic numerical simulations [17].

The experimental set-up consists of a mock-up, 20 temperature sensors, two pressure sensors and a flow meter. As a cooling liquid is used the demineralized subcooled water, which is pumped through the mock-up in a closed loop system. Block schematic of the set-up is illustrated in Figure 7. The 16 thermocouples (TC) type K with 1 mm diameter are positioned in the cavity wall at 4 different distances from the inner wall surface: 1.2 mm, 2 mm, 5 mm, and 6.5 mm. In the direction parallel to the mock-up axis, eight of these thermocouples are positioned in the centre plane ($z = 0$) and four TCs are placed in the planes $z = 15$ mm and $z = -15$ mm, respectively. Additionally, to 16 thermocouples, four thermal sensors PT100 (resistivity thermometers) are integrated in the inlets and outlets, in order to perform the calorimetry measurements [17].

Pressure sensors measure the pressures at the upper inlet and outlet, giving the pressure difference between them. One flow meter is positioned before the splitting of the water line into the two inlets and measures the total water flow. The experimental installation is depicted in Figure 8 [17].

MINAC 6® induction heater of the EFD Company provides the maximal heating power of 10 kW. The geometry of the inductor head is chosen to fit into the presented mini channels mock-up, to improve the efficiency of the induction heater and to fairly simulate the heat load spatial distribution in the coaxial gyrotron cavity. Outer diameter of the inductor head, with a one loop copper coil, is 57 mm (Figure 9), assuring a safe insertion of the inductor head into the mock-up with 59 mm inner diameter and reducing the possibility of hazardous touching of the inductor head and the mock-up inner wall. Additionally, the air gap of only 1 mm between the coil head and the inner mock-up wall maximizes the efficiency of the heating [17].

The acquisition system consists of the Siemens Simatic S7-300® CPU and analog input modules for a signal processing and of the Siemens software WinCC Runtime® for visualization and recording of the measured data. The test system has the acquisition frequency of 1 Hz [17].

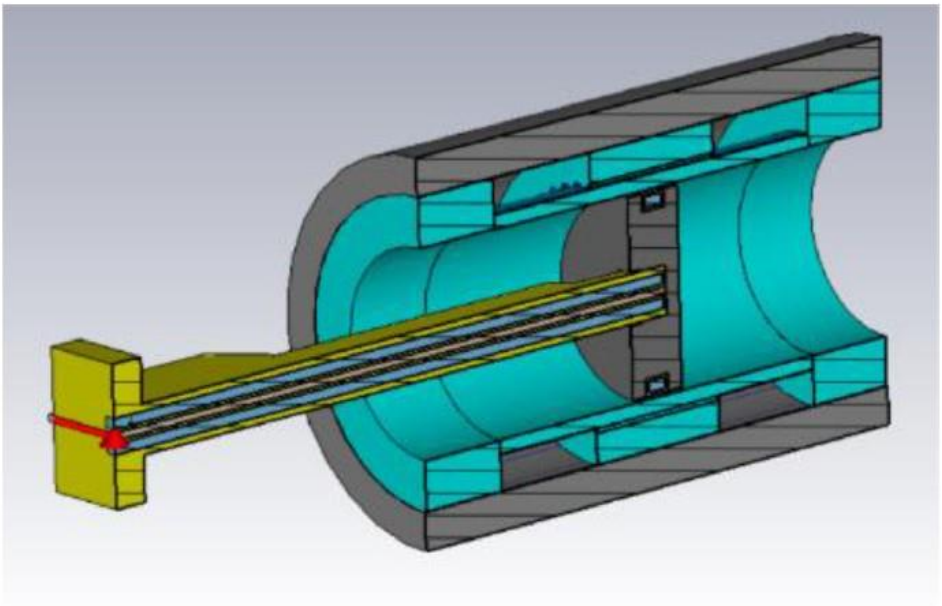

Figure 15. Model for EM simulations: mini-channel mock-up with inserted inductor heater head [17].

3.2 Thermal Model and Comparison to Dry Test Results

A pure thermal model of the entire mock-up has been first developed using the commercial software STAR-CCM+ [19], to check and calibrate the deposited power, computed by mean of an EM model as explained in [17]. For the computational grid, a polyhedral mesh with base size of 1.4 mm has been used. It is refined for the high heat load region in the resonator and water stopper with base size of 0.35 mm (Figure 16). A total number 3.6 M cells is obtained.

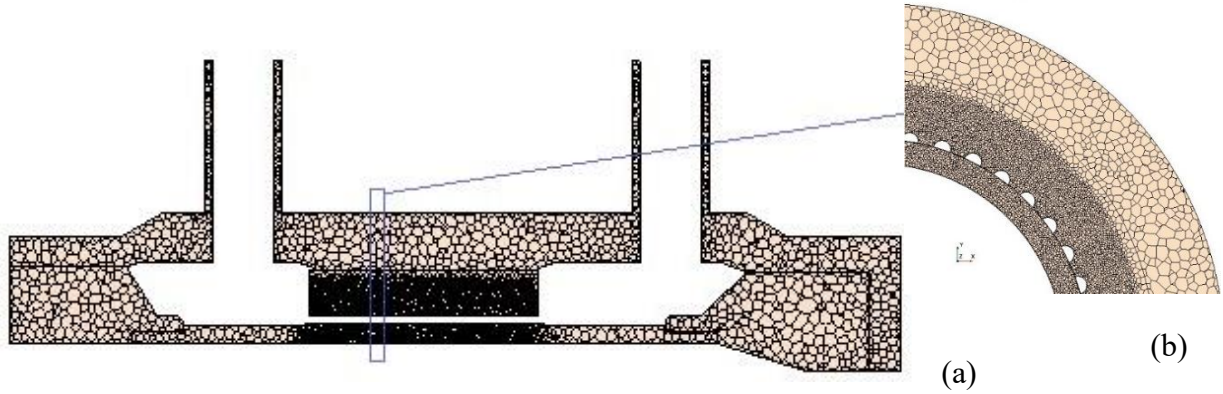

Figure 16. a) Polyhedral mesh on a longitudinal section of the upper half of the solid parts for the pure thermal model of the mock-up, and b) zoomed view on the transversal section highlighted in (a).

In the numerical model, the thermocouples are also inserted as suggested in L. Savoldi et al., "*Predictive simulations on mini-channels using the MUCCA tool for full-size cavity mock-up of KIT*", *EFDA_D_2PFSHG* 2021. Their base size is defined as 0.1 mm shown in Figure 17. The material of thermocouples is taken as stainless steel. The temperature at the TCs is computed as a surface average of a 0.1 mm diameter sphere positioned at the nominal location of the TCs, assuming perfect contact between the TC head and the copper surface. The TC bodies are considered up to mantel. Note that, in view of the asymmetric location/depths of the TCs, no simplification of the computational domain accounting for the geometrical symmetry was possible.

The thermal contact resistance on the solid interfaces between steel and copper surfaces is not imposed based on the study in *EFDA_D_2PFSHG*, which showed that those parameters have negligible impact on the computed results. All solid walls are considered adiabatic except the inner wall of resonator, see Figure 18.

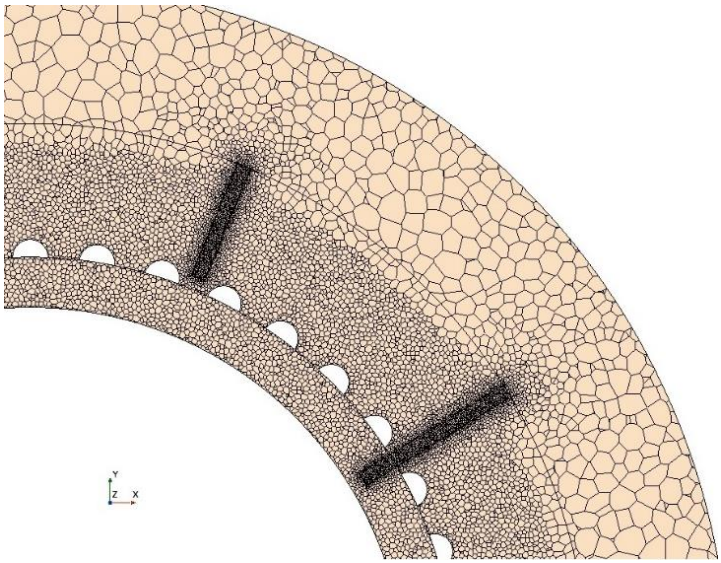

Figure 17. Zoom-in transversal section across two thermocouples located at different depths with respect to inner wall of resonator.

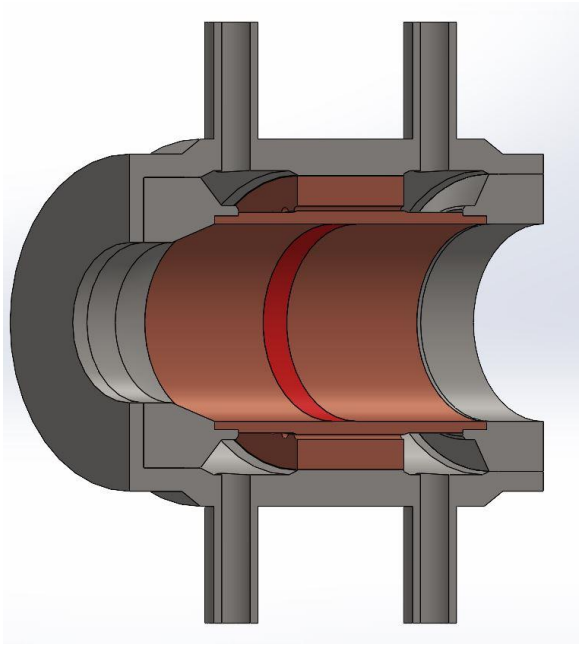

Figure 18. Setup of the thermal simulations: adiabatic boundary conditions are applied everywhere, except in the inner surface of the cavity, where the applied heat load peak is highlighted in red

The material properties for copper [19 21] and stainless steel [20 22] are taken as function of the temperature, as reported in Figure 19 and Figure 20, respectively.

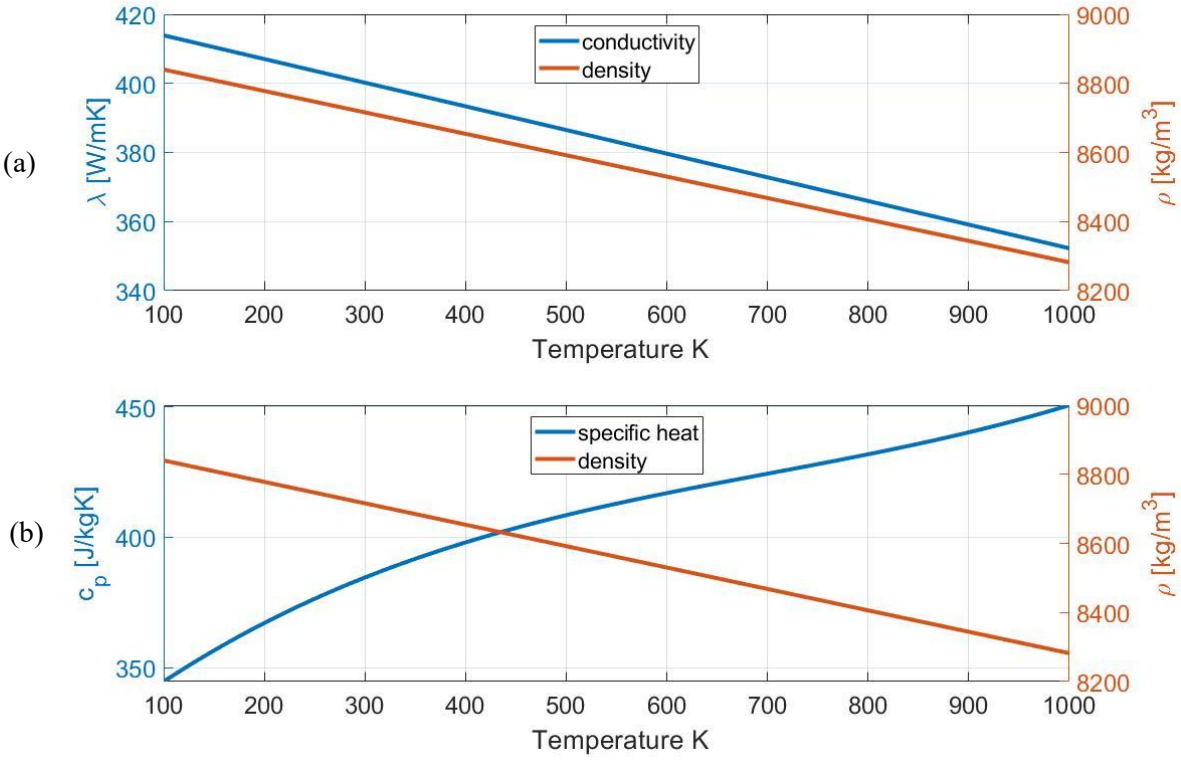

Figure 19. (a) Temperature dependence of copper conductivity λ and (b) specific heat cp and density ρ, as adopted in the numerical simulations.

(a)

(b)

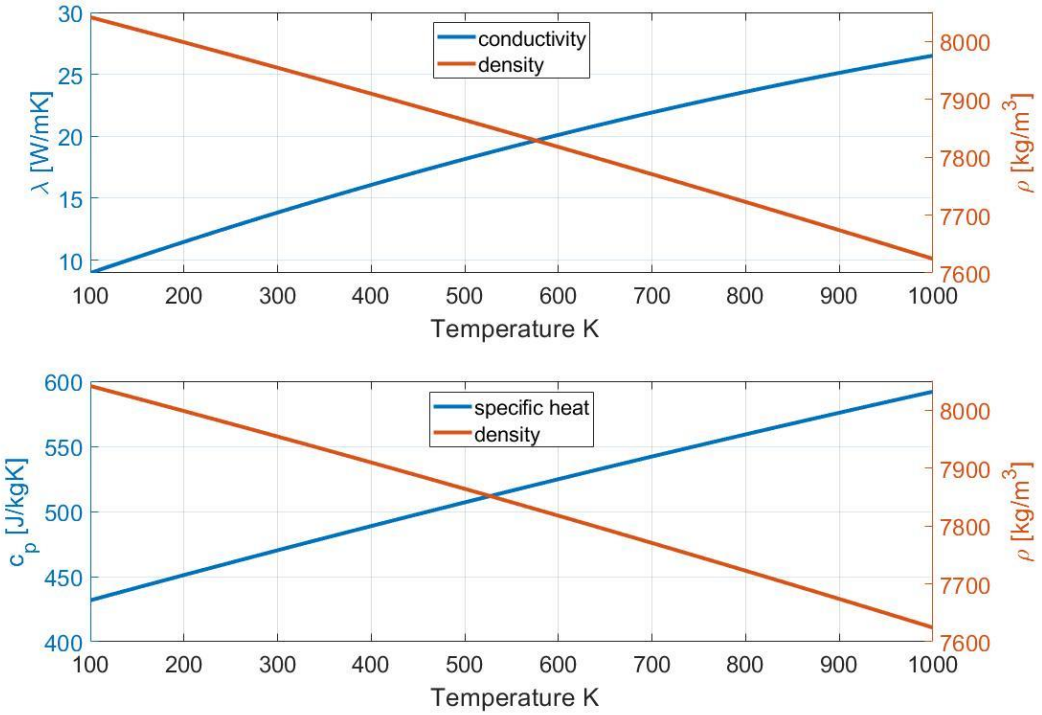

Figure 20. (a) Temperature dependence of stainless-steel conductivity λ and (b) specific heat cp and density ρ, as adopted in the numerical simulations.

The actual mock-up has been tested in transient without water flow with three different IH nominal power values Q_{IH} (600, 1200 and 1800 W) for ten minutes. In the test, power is deposited via an inductive heater on the resonator inner wall. An implicit unsteady model with time step equal to 0.1 s and 10 inner iterations has then been adopted to simulate 600 s of physical time. Simulations without cooling have run for three different power levels of the IH (Q_{IH} = 600 W,1200 W and 1800 W) for 600 s, using as driver the input power evaluated by the EM model developed at KIT by Dr. S. Stanculovic. The integral values of the deposted power are reported in the Table 1 for the different values of Q_{IH}, while the spatial distribution around and along the heated wall is shown in Figure 21. Note that the two highest values of Q_{IH} were not tested in dry conditions due to the excessive heating anticipated for the mock-up.

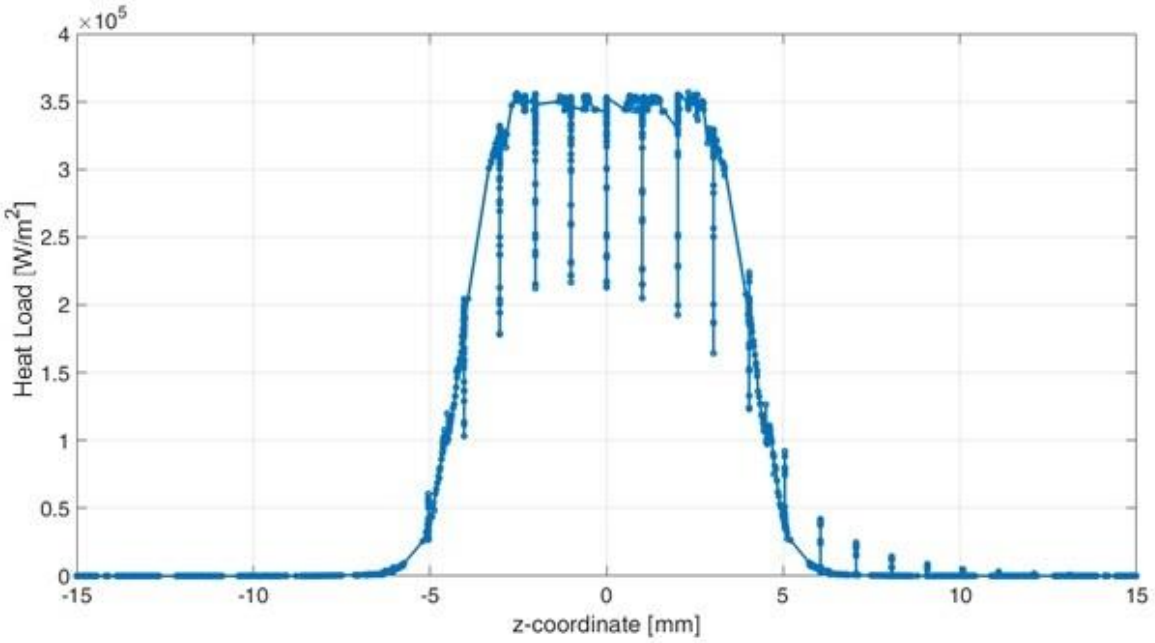

Figure 21. Longitudinal distribution of the heat flux computed by the EM simulations with Q_IH = 1800 W. The values at the same z refer to different azimuthal location around the heated surface.

Table 3. Integral value of the heat load on the inner wall as computed by the EM model, at different power level of the IH

IH nominal power Q_{IH} (W)	**Load (W)**
600	179
1200	356
1800	508
2400	701
3000	874

The temperature evolutions (both computed and measured) of the entire set of TCs for different power levels is summarized in Figure 22 below. It can be said that there is a good match between simulation and experimental results for Q_{IH} = 1200 W, while there is overestimation for Q_{IH} = 600 W and underestimation for Q_{IH} = 1800 W, respectively.

(a)

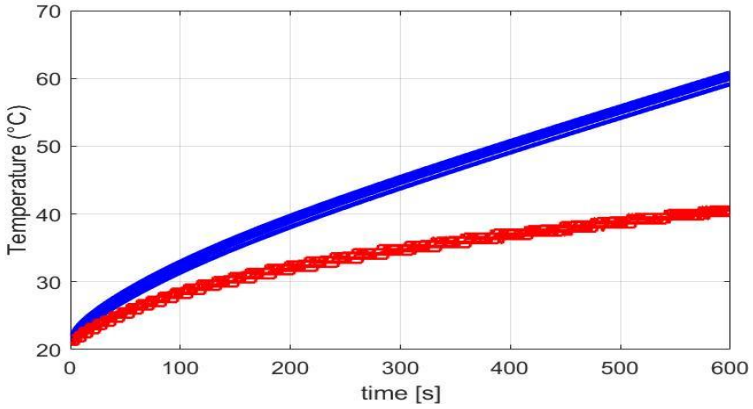

(b)

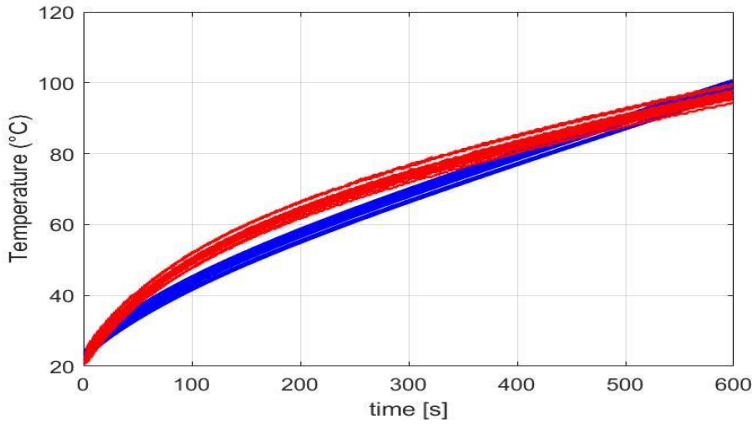

(c)

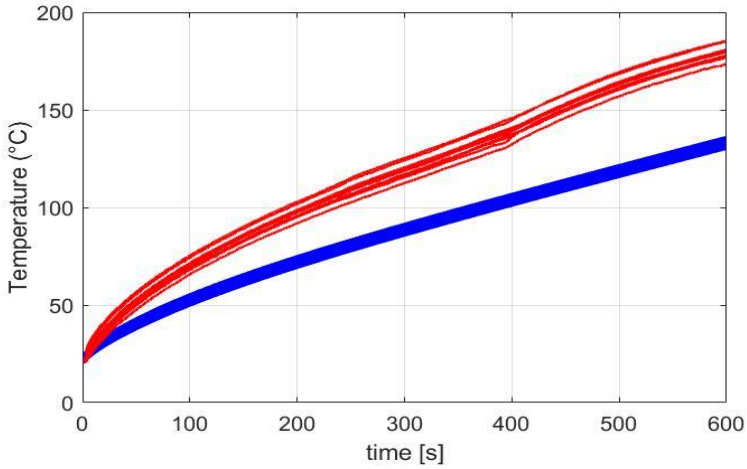

Figure 22. Temperature evolutions of TCs for a) Q_IH = 600 W b) Q_IH = 1200W c) Q_IH = 1800 W. Blue lines indicate simulation results, red lines the experimental results for all figures.

The difference in the temperature of thermocouples is clearly seen in the evolution, also in one-to-one comparison in Figure 23. Regardless of the position of thermocouple, all of them are significantly below what is expected from experiments. Also, the difference in the temperatures is similar for all TCs which could be an indication of a calibrated heat load might affect all the thermocouples in the same way. If in the outcome of simulations different behaviours of

thermocouples were observed, the validity of the model could have been questioned, but the disagreement here rather depends on a significant underestimation of the input power.

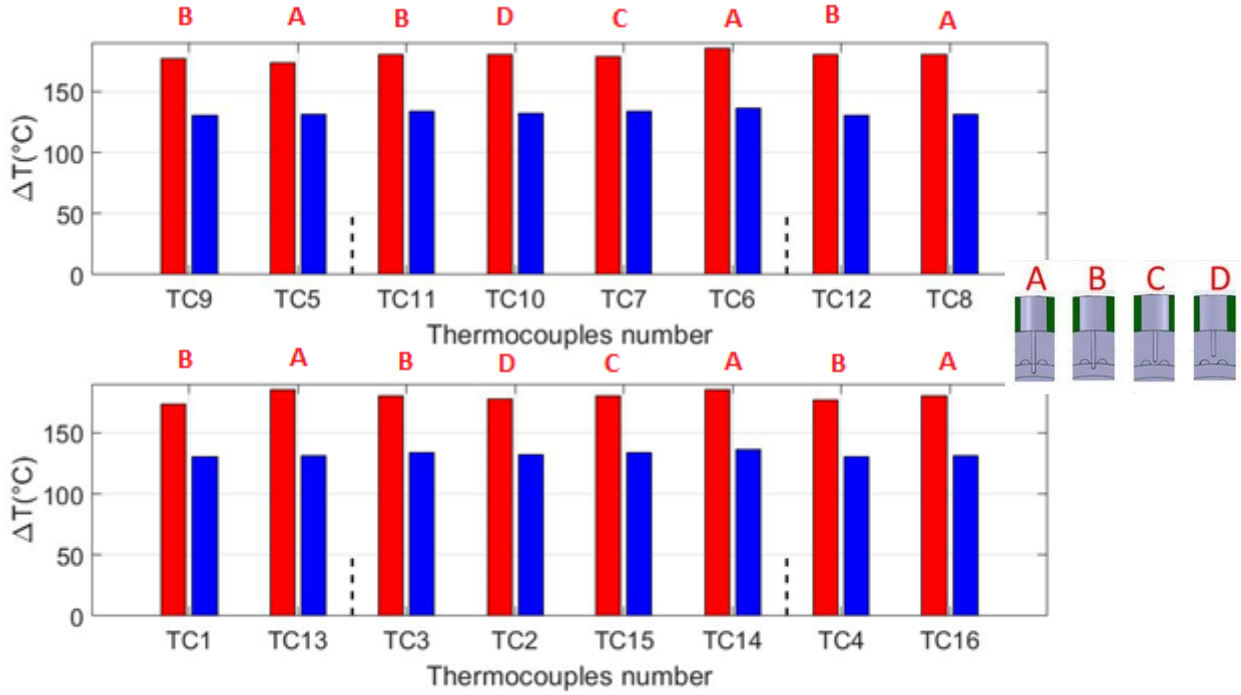

Figure 23. Thermocouple temperature comparison in the dry conditions, at 600s for Q_IH =1800. Blue bars indicate simulation results, red bars the experimental results. In the inset, the radial position of the Tc is reported.

It is clear that is not possible to drive a single calibration factor as was done in [17]. The calibration factor was aimed to be used in further thermal-hydraulic simulations, but since that is not a viable option here, another approach is followed for the calibration of heat load, i.e. relying on the experimental caloimetry to find a transfer function between the Q_{IH} and the heat load currently desposted in the mock-up.

3.3 Calorimetric Analysis of Tests with Water

The calorimetric assessment of the heat load on the cavity has been performed in order to check the heat load to be used in input to the thermal-hydraulic simulations. The calorimetry tests have been performed at different flow rates (10 and 20 l/min) and varying Q_{IH} (1800 W, 2400 W and 3000 W). The heat load computed from the experimental calorimetry with Eq. (1)

$$Q_{cal} = \dot{m}^{exp} \times c_p \times \left(T_{out}^{exp} - T_{in}^{exp}\right) \quad (1)$$

where Q_{cal} is the heat load calculated from the experimental results, $\dot{m}^{exp}$ is the total water mass flow rate in the mock-up, c_p is the water specific heat, T_{out}^{exp} and T_{in}^{exp} are the outlet and inlet temperatures of the water, averaged on the two measured values at the inlets and two outlets of the mock-up. The measured values have been averaged over the last tens of second for each test.

In Figure 24, the calorimetric power evolution in time for $Q_{IH} = 1800$ W is reported. As it can be seen, after reaching steady-state condition, some fluctuations are evident. In order to consider these fluctuations, an uncertainty propagation analysis is performed.

Table 4. Input measured data for the calorimetric evaluation of the power, and measured water inlet pressure

$\boldsymbol{Q_{IH}}$ [W]	$\boldsymbol{T_{in}^{exp}}$ (◦C)	$\boldsymbol{T_{out}^{exp}}$ (◦C)	$\boldsymbol{\dot{m}^{exp}}$ (l/min)	Inlet Pressure (bar)
1800	13.4	14.2	10.1	2.5
	16.3	16.8	19.9	2.7
2400	13.2	14.6	10.1	2.5
	12.8	13.4	20.4	2.7
3000	12.8	15	10.1	2.5
	12.8	13.9	20.4	2.7

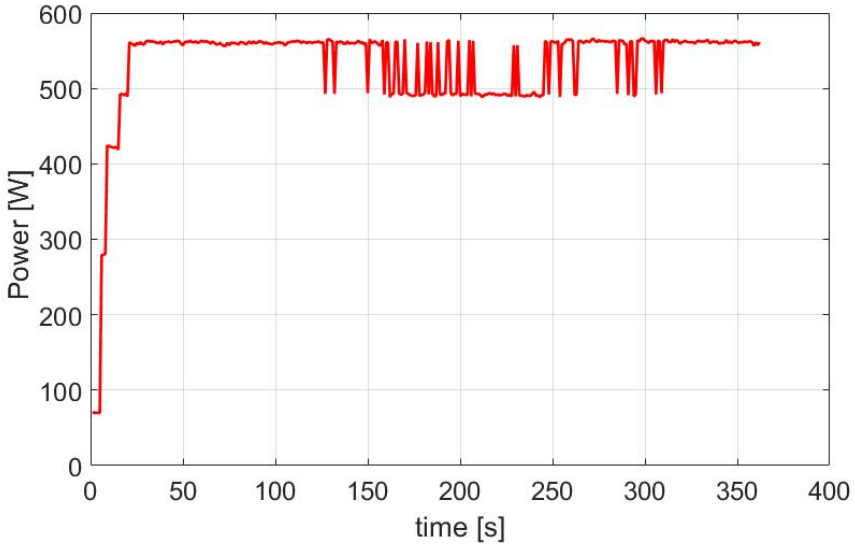

Figure 24. Calorimetric power evolution at 1800 W inductive power for 10 l/min flow rate

The uncertainty propagation is calculated based on the measurement equipment sensitivities where temperature sensor's uncertainty (u_T) is equal to 0.2 K and for the flow rate (u_m) is 0.025 kg/s, as reported by the instrumentation instructions [S. Stanculovic, private communication, 2020]. For this calculation the specific heat of water is considered as constant.

$$u_{total} = \sqrt{\left(\left(\frac{dQ}{dT}\right)^2 \times u_T^2 + \left(\frac{dQ}{dm}\right)^2 \times u_m^2\right)} \tag{2}$$

The total uncertainty (u_{total}) is the sum of the contributions of the uncertainty in the temperature and flow rate measurements calculated with equation (2) where , $\left(\frac{dQ}{dT}\right)^2$ is square of the derivative of Q with respect to temperature, u_T^2 is square of the uncertainty of temperature, $\left(\frac{dQ}{dm}\right)^2$ is square of the derivative of Q with respect to the flow rate and u_m^2 square of the uncertainty of flow rate. The two derivatives of Q represents the sensitivity coefficients of the uncertainty propagation study and are evaluated as analytical derivatives respectively with respect to temperature and flow rate. The value is obtained by assigning the known values of c_p, flow rate and temperature differences in the different cases.

The results of the calorimetric assessment with uncertainty ranges in comparison with integral power from EM model and integral power evaluated in the simulation is represented in Figure 25 and in Figure 26.

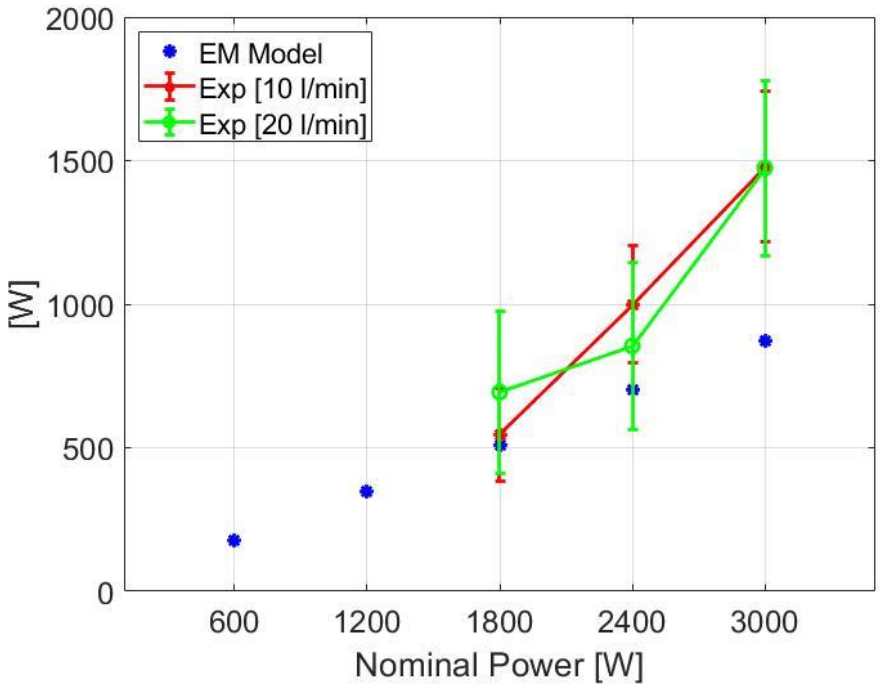

Figure 25. Calorimetric power at different water flow values with its error bar, compared to the integral power from EM model (stars).

Table 5. Calorimetric Power with Uncertainties at different nominal power levels in comparison with Integral Powers from EM model and simulation.

Q_{IH} (W)	**Power at 10 l/min (W)**	**Power at 20 l/min (W)**	**Average power (W)**
1800	544 ± 162	693 ± 282	619
2400	1000 ± 205	855 ± 292	928
3000	1479 ± 261	1475 ± 305	1480

The difference in the integral power values evaluated from EM model and simulations is due to numerical error in the computer evaluation. Since there are two calorimetric powers calculated at each nominal power level, the average of calorimetric power is compared to EM model integral power in Figure 18. It is clear that the power computed from calorimetry is progressively much higher than the one computed using the EM model, as the nominal power level of the inductive heater Q_{IH} increases. In Figure 26, also the power computed from calorimetry in the 2020 test campaign [17] is reported. If the purpose of switching from Glidcop

to Copper as cavity material was to increase the actual heat load to the cavity, it is clear that the target was not achieved, being the 2021 power levels lower that the 2020 ones [17], for the same Q_{IH} (see also Table 4). The 2020 calibration data [17] are barely within the uncertainty bar of the 2021 calibration (not shown but clear from Table 5).

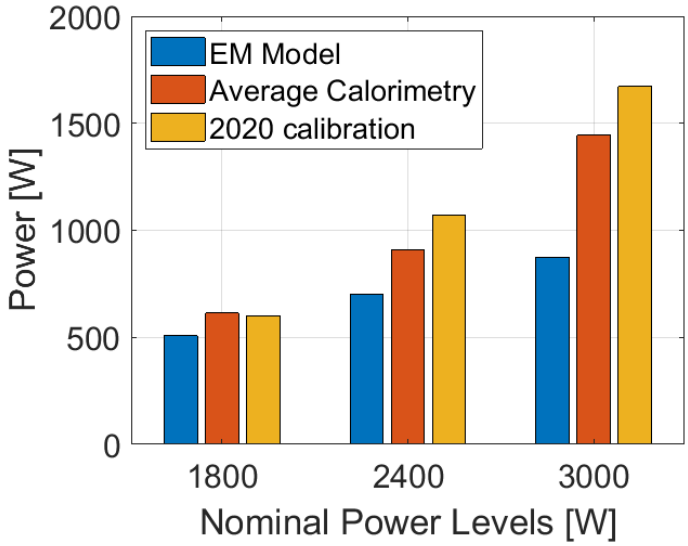

Figure 26. Average calorimetric power in comparison with EM mode and compared to the integral values of the calibrated heat load obtained in 2020 [17] work.

3.4 Calibration of The Input Power

Thanks to the experimental calorimetric evaluation, it was possible to derive transfer function between the Q_{IH} and the heat load currently desposted in the mock-up. Based on the ratio computed for Q_{cal}/Q_{EM}, a parabolic transfer function was computed, shown in Figure 27-a. As a comparison, the heat load shape computed in 2020 [17] is also reported, showing a less pronounced peak in the middle region and a higher load in the region upstream of the load peak.

The computed fit was used to correct the values of Q_{EM} in order to compute load values compliant with the experimental results. In Table 6 the corrected values are reported for the entire set of Q_{IH} for the sake of completeness. Note, however, that the two lowest Q_{IH} values are obtained by extrapolation from the calibration range and are not to be considered reliable.

Table 6. IH Nominal power, EM Model power and Calibrated Power according to the computed parabolic fit. The 2020 calibration results are also reported for the sake of comparison.

Q_{IH} (W)	EM Model power (W)	Calibrated (Expected) power (W)	2020 calibrated power (W) [17]
600	*179*	*208*	
1200	356	*414*	
1800	508	619	602
2400	701	928	1069
3000	874	1480	1671

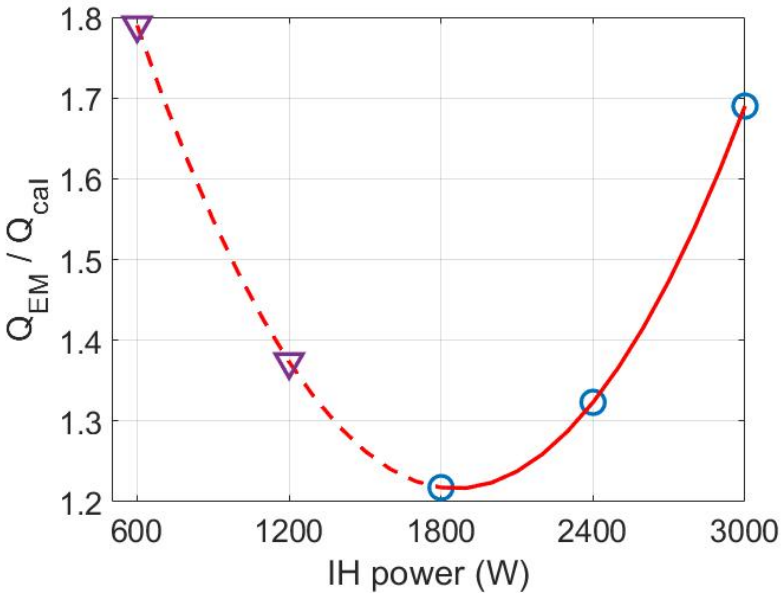

(a)

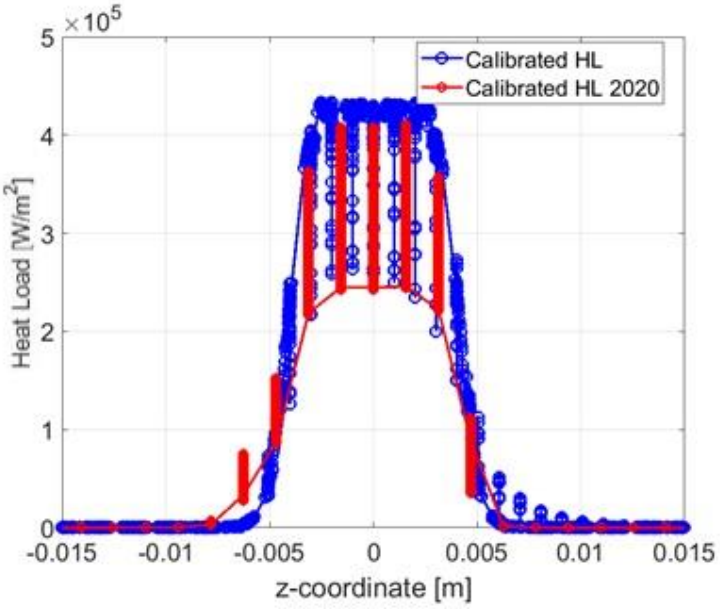

(b)

Figure 27. (a) Parabolic fit for the Q_EM multiplier at different Q_IH (open circle: calorimetry data, open triangles: extrapolated data) (b) Spatial distribution of the calibrated heat load for Q_IH = 1800 W.

3.5 Validation of The Calibrated Input Power

The calibrated heat load reported in Figure 27-b is used as input for dry (pure thermal) simulation in order to verify the recipe of parabolic fit. In Figure 28, the thermocouple temperature comparison of experimental and simulation results at 600s for the calibrated 1800 W heat load is reported. The simulation results are much closer to measured ones compared to the initial case where no scaling has been applied to heat load (see Figure 23). In addition, the integral power evaluated in the simulation is 625 W, matching well the expected outcome of calibration reported in Table 6. The average relative error of the TC at 600 s is below 6%, with ε_{rel} computed on each TC as in Eq. (3).

$$\varepsilon_{rel} = \left| \frac{T_{exp} - T_{comp}}{T_{exp} - T_{initial\_exp}} \right| \quad (3).$$

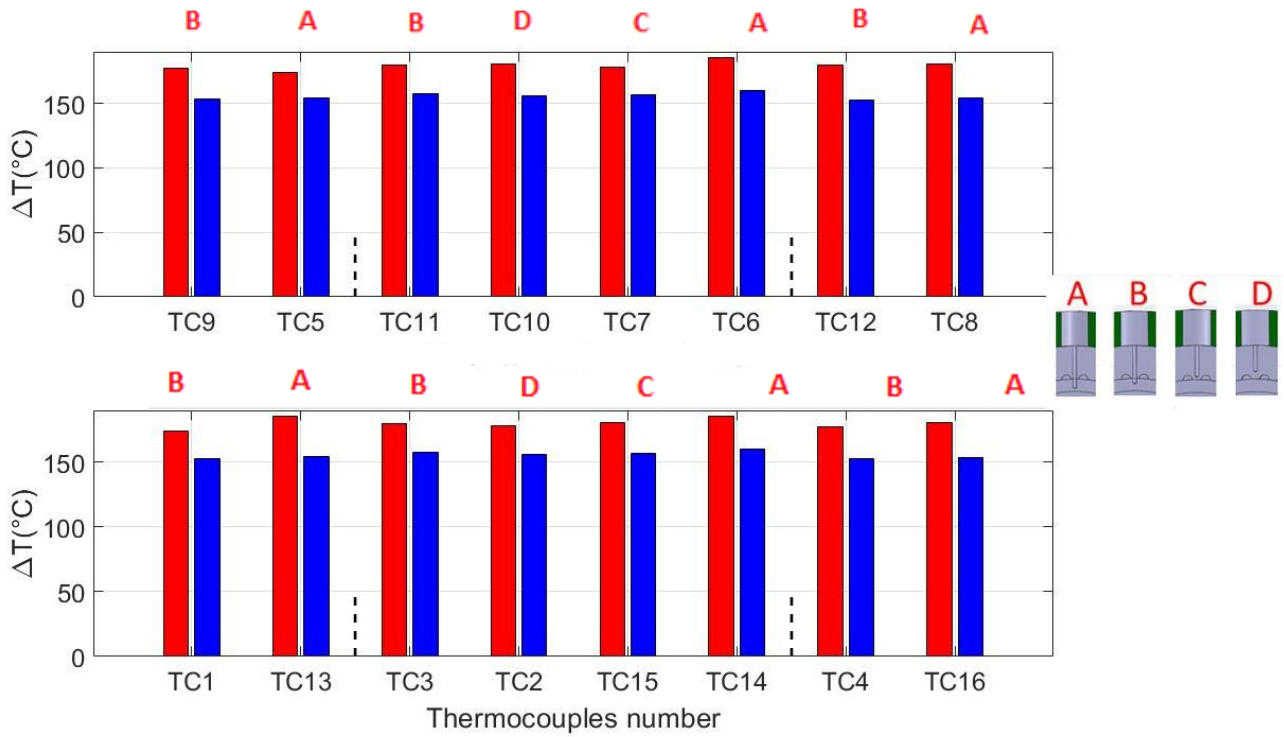

Figure 28. Thermocouple temperature comparison at 600s for Q_IH =1800. Blue bars indicate simulation results, red bars the experimental results.

3.6 Analysis of Mock-Up Tests with Water

3.6.1 Thermal-hydraulic model

The 3D steady-state conjugate thermal-hydraulic model has been then developed for the entire mock-up, including the coolant, using the commercial software STAR-CCM+. Since the mock-up is cooled by water entering the cooling region by two different inlets in parallel, the model for the thermal-hydraulic simulations also includes T-junctions upstream and downstream of the mock-up to allow the balance of the flow computed in the two branches, see Figure 29.

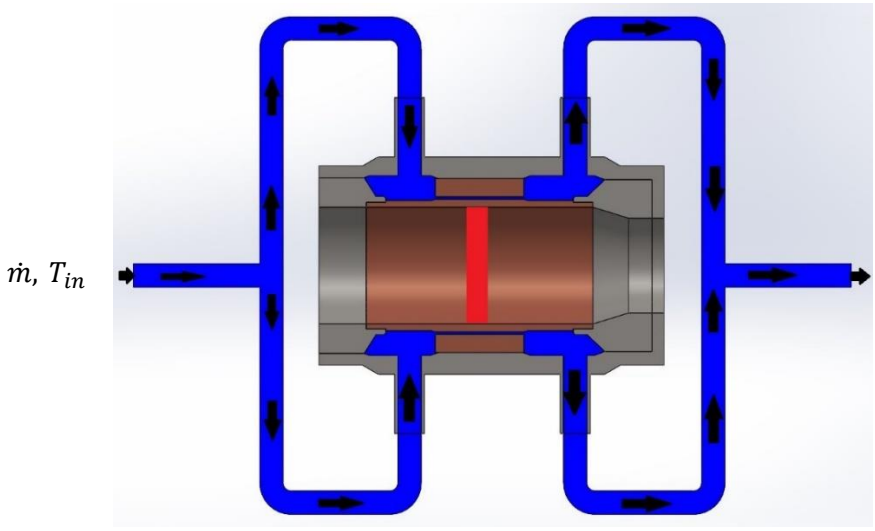

Figure 29. Sketch of the reference geometry for the full 3D thermal-hydraulic simulations, also including the water domain (in blue). Half of the computational domain is shown. The heat load peak is applied in the red region.

The k-ε Lag EB turbulence model, with all y^+ wall treatment, is adopted in the simulations since it can capture the flow detachment downstream of the mini-channels region. This turbulence model has been already demonstrated to be the best, among advanced k-ε and k-ω models, for the simulation of the hydraulic performance of mini channels [20]. For the solid domain, the same model described in Section 3.2 has been used.

The mesh built in the fluid domain account for 13M cells, and 5M for solid parts in total 18M of cells is obtained (Figure 30). The base size is defined as 3 mm then refined in channels, resonator, TCs and water stopper as 0.15 mm, 0.5 mm, 0.15 mm, 0.8 mm respectively. The

thickness of the first wall prism layer has been defined in order to obtain a dimensionless wall distance $y^+ \sim 1$.

The conjugate heat transfer problem is solved in steady state using a segregated solver. The thermal driver has the same spatial distribution computed with the EM model, scaled using the factors computed in the calibration study (see above). An inlet water mass flow ($\dot{m}$) of 0.34 kg/s (corresponding to 20 l/min) at 13.4°C (T_{in}) and 2.5 bar is used as inlet condition for the fluid domain, as shown in Figure 29. The water properties in the model are selected as IAPWS-97. Note that only the dataset at the highest flow rate could be used with the adopted turbulence model, since the lowest flow rate value would result in the transition regime.

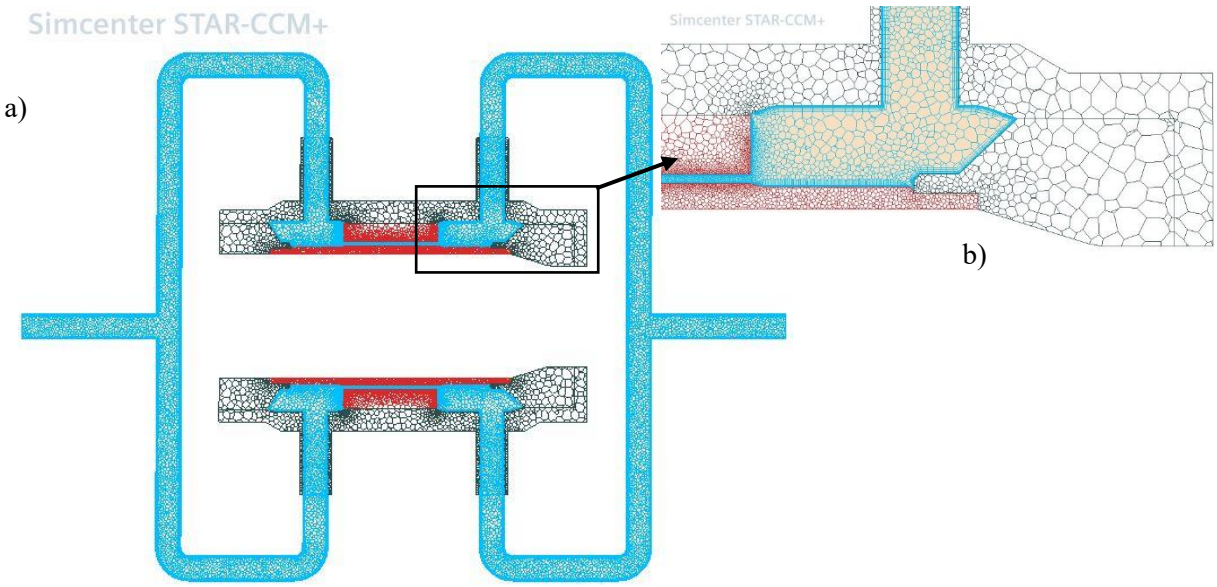

Figure 30. Polyhedral mesh of the a) longitudinal section of the solid and fluid part, and b) zoomed in view of the channel outlet region.

3.6.2 Computed results and comparison with experimental results

After calibration of heat load is performed (as described in section 3.4), temperatures measured with the different 16 TCs are compared with those computed in the steady-state simulations in Figure 32, Figure 33, and Figure 34 for 20 l/min mass flow rate at three different values of Q_{IH} (1800 W, 2400 W and 3000 W, respectively).

In all the three cases, a general good agreement between measured and computed temperatures in the middle section (i.e., corresponding to the surface that is directly heated) and underestimations at sections upstream and downstream the heated one are observed. Notice that the TCs located in the middle section measure in all cases higher temperature differences than the ones located in upstream and downstream position, since they are nearer to the heat load pick (highlighted red surface in Figure 18). Moreover, the TCs number 11, 6 in the top row and 3, 14 in the bottom row are located close to the inner wall of the cavity and measure the highest temperature increase in each case both in the experiment and in the simulations.

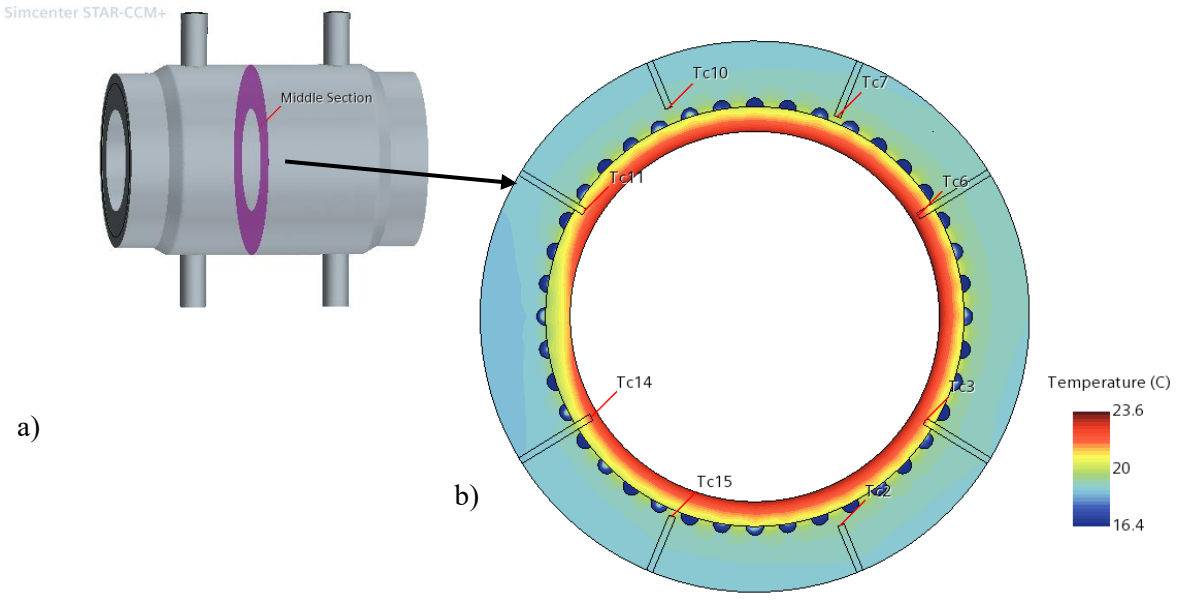

Figure 31. a) Highlighted: Transverse section across the mock-up where TCs 2,3,6,7,10,11,14 and 15 are located, b) Temperature map computed across the section in (a), also showing the TC location.

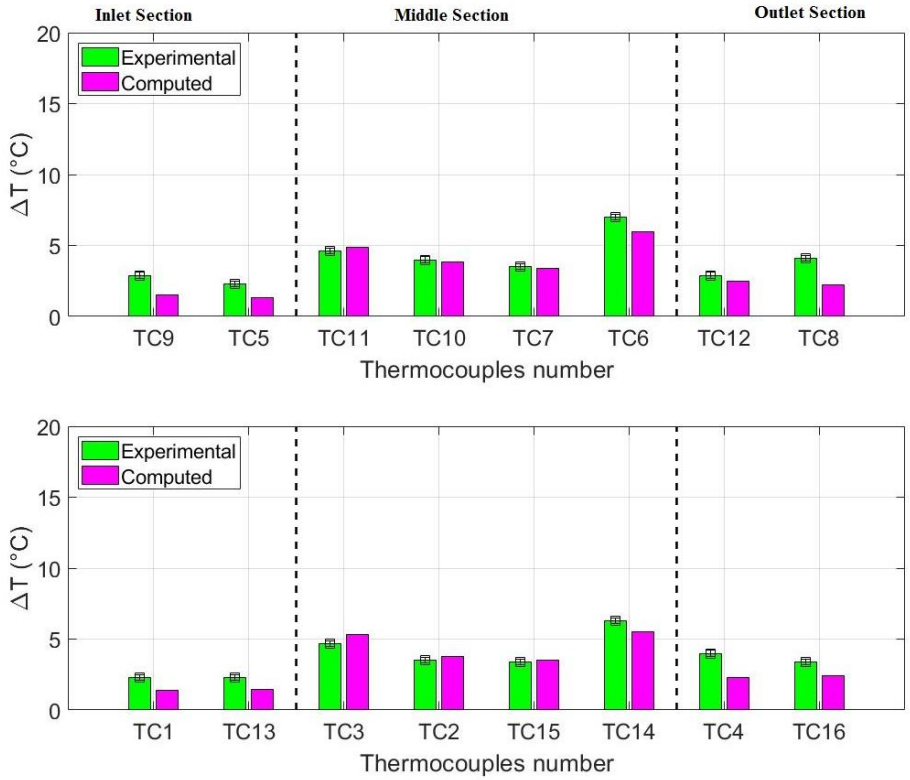

Figure 32. Test with water 20 l/min and QIH = 1800 W: comparison of experimental and computed TC temperature increases at steady state.

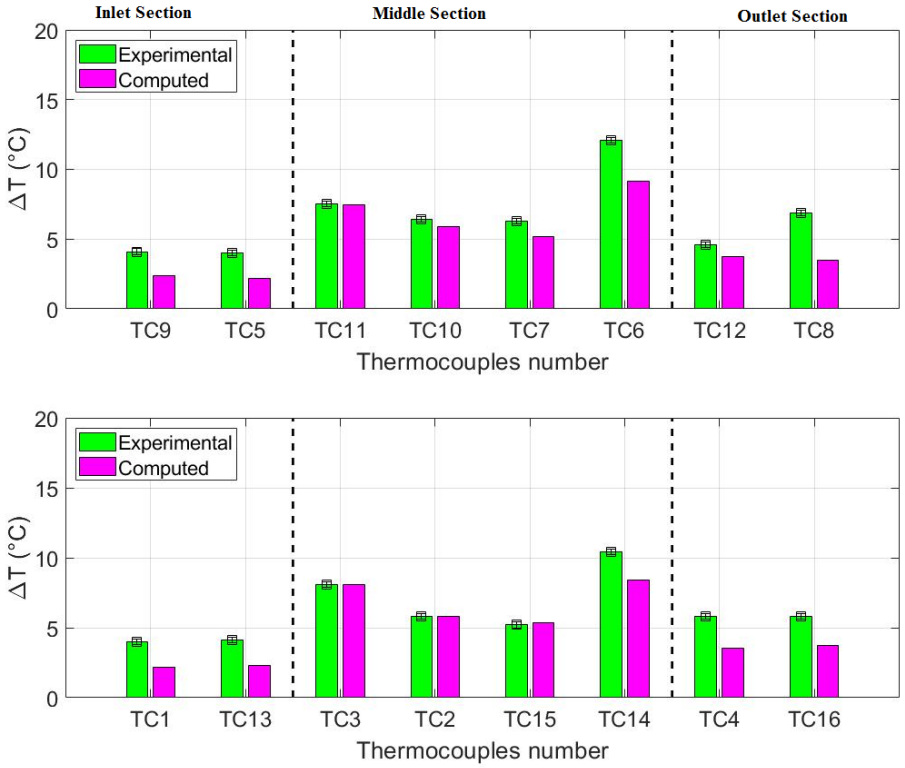

Figure 33. Test with water 20 l/min and QIH = 2400 W: comparison of experimental and computed TC temperature increases at steady state

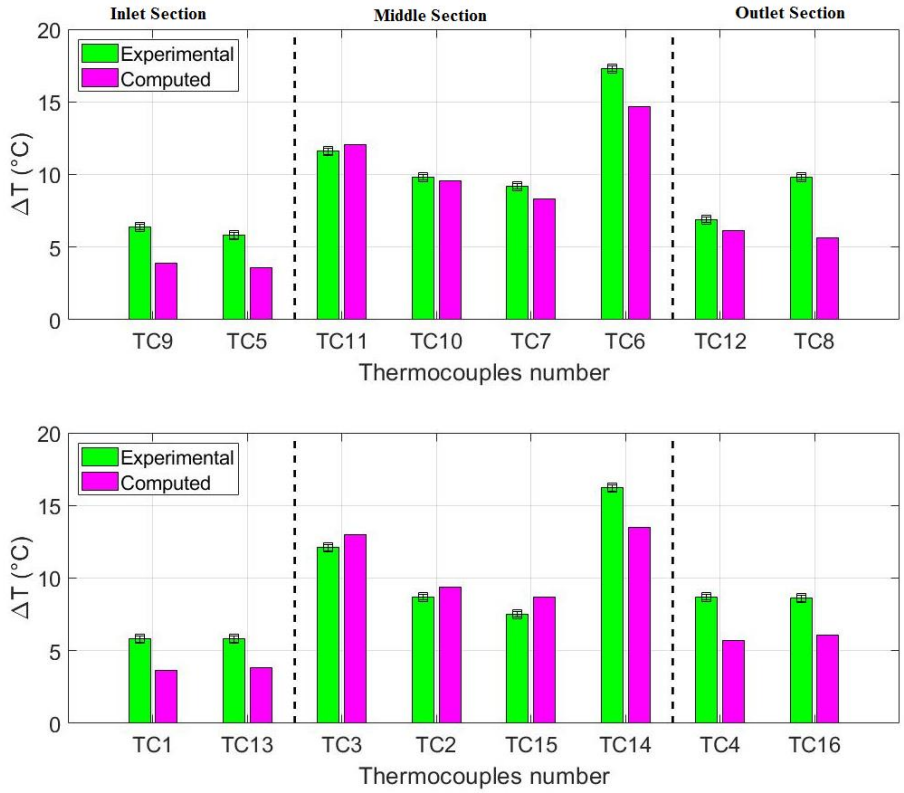

Figure 34. Test with water 20 l/min and QIH = 3000 W: comparison of experimental and computed TC temperature increases at steady state.

Concerning TC3, TC11 and TC6, TC14; even though they are placed at the same distance from the heated surface of the cavity and located at the same longitudinal coordinate, they show different readouts both tin the experimental and in the computed values. This is due to the fact that the heat flux is not fully axis-symmetric (see Figure 21), and namely it is lower close to the location of TC3 and TC11, which in fact show lower values than TC6 and TC14.

The underestimations in the inlet and the outlet sections could be the result of the uncertainty in the heat load distribution. While the integral values have been verified with the calorimetry, the effective azimuthal and longitudinal distributions present uncertainties due to the calibration procedure adopted. Other uncertainties could be due to the modelling of the TCs in simulation since it is difficult to determine the exact contact surface between the solid parts and TCs.

In Figure 35, a comparison between current and past [17] experiments and computations are reported. In the results from 2020 [17], the highest temperature differences are measured by TCs 11, 6, 3 and 14, while in the 2021 experiments the highest temperature differences are observed in the upstream and downstream sections. Some discrepancies can be observed in the

measured temperature differences between the two experimental campaigns. This could be explained by the slightly different heat load deposited due to the different material used for the cavity, which was Glidcop in the old mock-up and copper in the current one. The calibrated heat load in 2020, confirmed by the calorimetry measurements, for 2400 and 3000 W, was higher of ~15% of the current values. Note that most of the computed temperature differences, this year, are lower than the measured values, while in 2020 [17] it was the opposite.

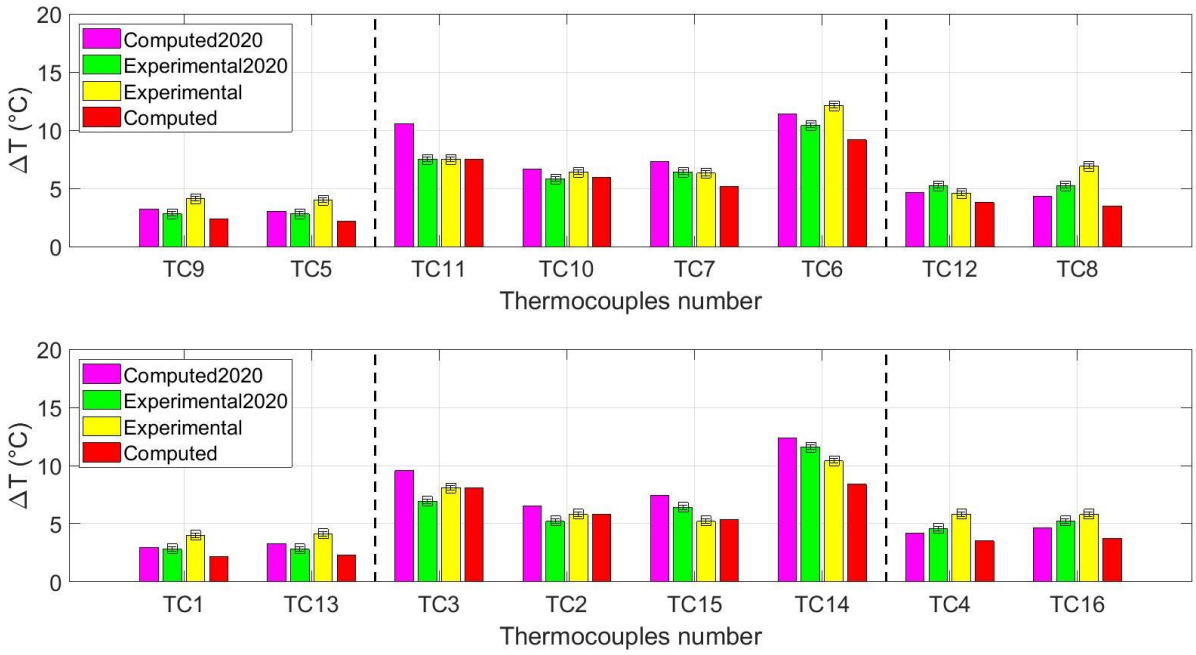

Figure 35. Comparison between current experiments and 2020 ones [12] for 20 l/min of flow rate and 2400 W of inductive power. Measured and computed temperature differences are represented.

More in detail, the relative errors evaluated with respect to the measured temperature differences are reported for each 2021 test case in Figure 36. As seen in Figures 32, 33 and 34, the underestimations in the upstream and downstream, sections of the mock-up resulted in high relative error up to 50%. On the other hand, the middle section, where the heat load is applied, the gap closes between experimental and computed values and the relative error remains below 20%.

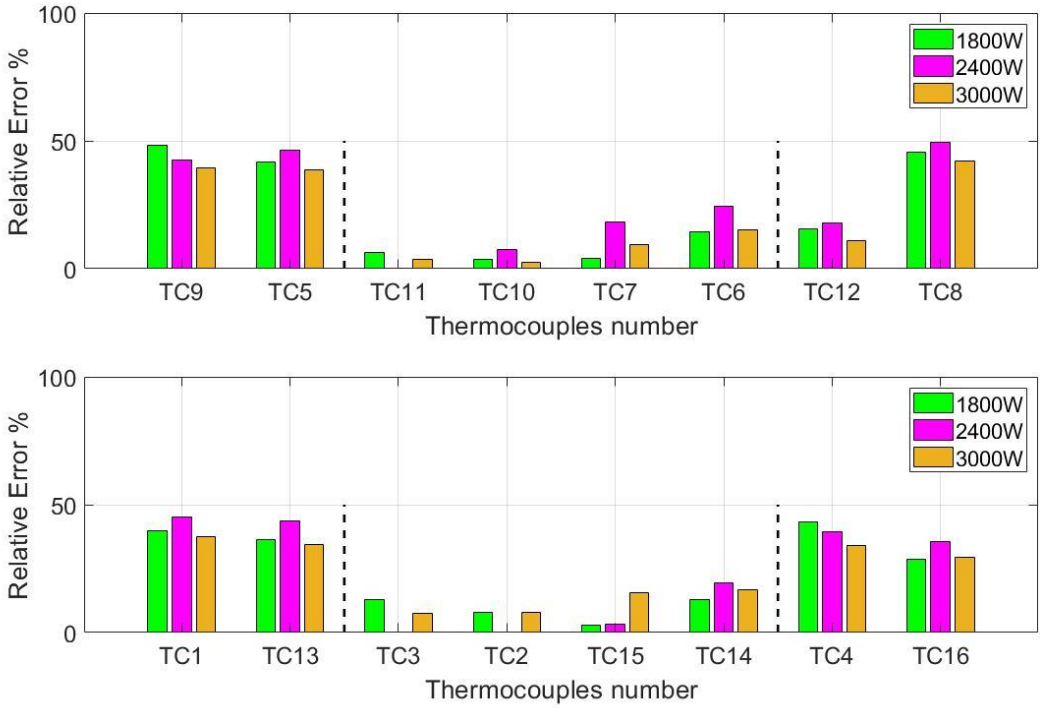

Figure 36. Relative errors evaluated with respect to the measured temperature differences for all TCs in 1800, 2400 and 3000W.

One possible explanation for the underestimation of the temperature differences in the TCs in the middle section is the perfect thermal coupling (corresponding to a contact resistance $R_{th} = 0$) between the cavity and the water-stopper, adopted so far in the simulations. Note that, while no thermal resistance was considered in the 2020 [17] simulations, a thermal resistance of 1×10^{-5} m^{2}K/W was already used (and actually needed) in the simulation of the planar mock-up tests to reproduce the experimental data [15]. The effect of the R_{th} on the simulations results has been analysed by varying its value in different simulations. The values have been chosen in a range of copper/copper thermal contact resistance. The absolute values of the relative errors evaluated for each TC in the different cases simulated are represented in Figure 30. Increasing the values of the R_{th} the relative errors in the central region increase while the general trend in the upstream and downstream region is to decrease. The obtained temperature differences for the cases with $R_{th} = 1 \times 10^{-5} \frac{\mathrm{m^2K}}{\mathrm{W}}$ and $R_{th} = 5 \times 10^{-5} \frac{\mathrm{m^2K}}{\mathrm{W}}$ are reported in Figure 37. We can observe that with $R_{th} = 5 \times 10^{-5} \frac{\mathrm{m^2K}}{\mathrm{W}}$ there is no underestimation of the temperature difference in the central TCs located in the cavity (TCs 11, 6, 3 and 14) while an underestimation observed for central TCs with head in the water stopper (TCs 10, 7, 2 and 15).

These results suggest the need of a study of the value of the R_{th} also between the other solid parts – this issue will be addressed in future simulations.

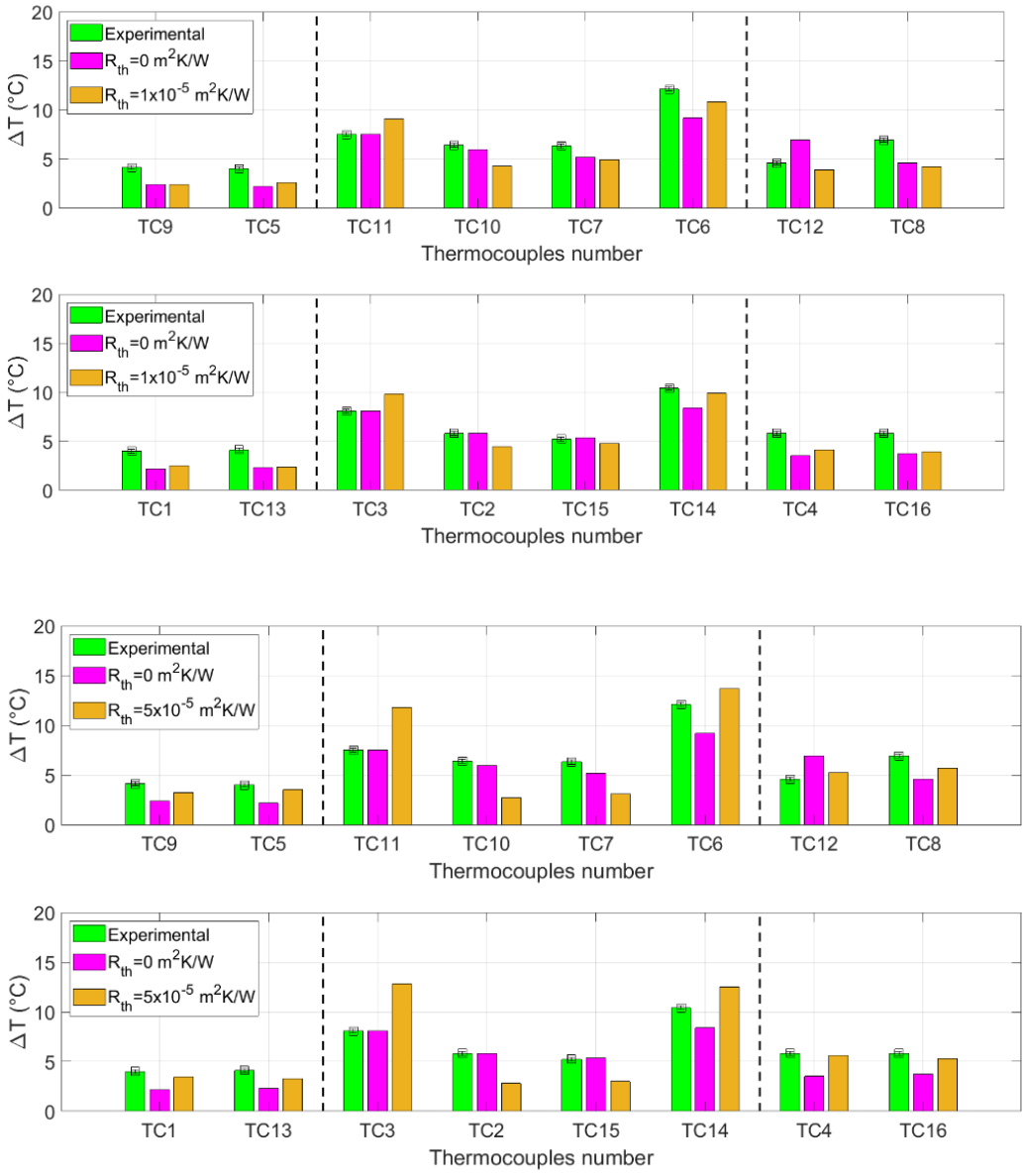

Figure 37. Temperature differences with (a) R_th=1×10^(-5) (m^2 K)/W and (b) with R_th=5×10^(-5) (m^2 K)/W for 2400 W compared to null R_th and experimental results.

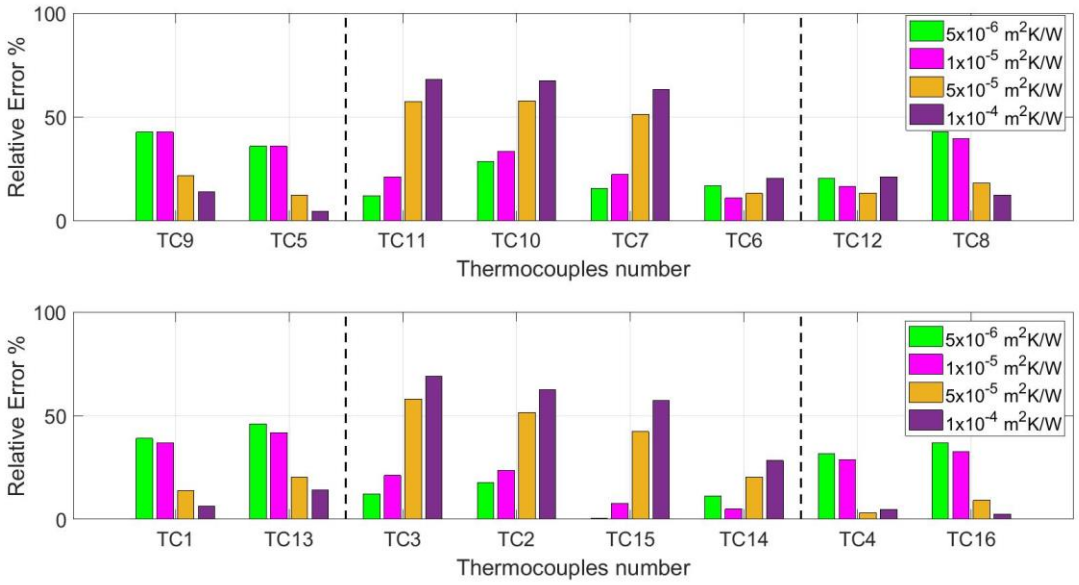

Figure 38. Relative errors evaluated with respect to the measured temperature differences for all TCs with different values of R_th for 2400 W.

The overall picture of the effect of the progressive increase of R_{th} on the computed errors for the temperature computed at the TC location is summarized in Figure 38, showing that a R_{th} value between $1 \times 10^{-5} \frac{\mathrm{m^2K}}{\mathrm{W}}$ and $5 \times 10^{-5} \frac{\mathrm{m^2K}}{\mathrm{W}}$ would possibly be the best compromise between a very good agreement in the middle section of the cavity and a god agreement in the upstream/downstream sections. To give the flavour of the effect of the R_{th} on the transient results, the value of $R_{th} = 5 \times 10^{-5} \frac{\mathrm{m^2K}}{\mathrm{W}}$ will be used in the simulations with air, because it gives the larger effect on the temperatures computed in the middle section of the cavity.

3.7 Conclusions

Firstly, the hydraulic performance analysis of a mock-up equipped with mini channels realized by additive manufacturing at THALES has been performed. The experiments to determine pressure drops at different flow rates are performed at THALES using water as the fluid. The experimental results are then compared to 3D – CFD simulation results in order to verify the numerical model. Due to unexpected issues, thermal-hydraulic experiments could not be performed hence, analysis of cooling performance of additively manufactured mini channels could not be evaluated.

It is clear that the model of mock-up equipped with mini channels is successful hydraulically, in terms of reproducing the pressure drops. It is a promising result for further thermal-hydraulic evaluations since pressure drop is a significant issue for heat exchangers.

Secondly, the analysis of the tests of a cavity sample using the KIT inductive heater are analysed in the case of no active cooling (dry sample) and cooling with water. The heat load distribution was received as input from KIT, where it was computed by means of an EM model. A first comparison of simulations and experimental results in the case of the dry cavity showed a significant discrepancy of the computed temperature signals, which called for a recalibration of the overall deposited power. Analysing the water measurements, the total amount of heat load deposited for the available inductive power levels (1800, 2400 and 3000 W, respectively) was evaluated by calorimetry, together with its uncertainty. The heat load profile obtained with the EM model was then scaled to the calorimetric power, keeping the spatial distribution computed by the EM model unchanged – the recipe was cross-checked by simulations of one of the dry tests, giving a reasonable agreement with the measured temperature traces.

The CFD simulations of the conjugate heat-transfer problem with water as coolant were then performed in steady condition. The simulations with a perfect thermal contact between the cavity and the water stopper returned an acceptable agreement between the temperature increase computed at the TC location in the steady simulations. A parametric study on the value of the contact thermal resistance R_{th} between the cavity and the water stopper allowed improving the agreement. Note, however, that a precise fitting value for that parameter within the range $1 \times 10^{-5} \frac{m^2 K}{W} - 5 \times 10^{-5} \frac{m^2 K}{W}$ has not been found yet because of the lack of time.

Moreover, the need to also assess the effect of finite (non-null) contact thermal resistances between the different solid components is now clear.

The simulations performed so far highlight the need for a more accurate EM model to compute the spatial distribution and amount of heat deposited in the cavity – the global calorimetry based on experimental data could in fact only contribute to confirm the total power deposited in the cavity but cannot help in suggesting its spatial distribution.

Moreover, if the rational of moving from a Glidcop sample [17] to a fully copper sample (tested in 2021 with the same design and layout of the 2020 mock-up [17]) was to reach higher effective heating on the mock-up, the analysis of the test results unfortunately showed that the expectation was not met by the samples, since the 2021 deposited power was, for the same levels of the inductive heater power, lower than the 2020 [17] deposited power.

The results of this study have been presented in an international symposium under the name of "Assessment of different RANS turbulence models in the thermal performance of mini-channels for the cooling of MW-class gyrotron resonator" at American Society of Mechanical Engineering – ASME Verification & Validation Symposium 2022.

References

[1] https://www.iter.org/proj/inafewlines

[2] https://www.iter.org/mach/heating

[3] https://www.epfl.ch/research/domains/swiss-plasma-center/research/tcv/research_tcv_heating/tcv-ecrh-eccd-system/tcv-gyrotrons/

[4] Kandlikar, S.G., and Grande, W.J., 2002, "Evolution of Microchannel Flow Passages – Thermohydraulic Performance and Fabrication Technology," Paper No. IMECE2002-32043, International Mechanical Engineering Conference and Exposition 2002, New Orleans, Nov. 17-21, ASME, also being published in Heat Transfer Engineering, Vol. 25, No. 1, Jan. 2003.

[5] Kandlikar, Satish G. "Microchannels and minichannels–history, terminology, classification and current research needs." *First International Conference on Microchannels and Minichannels*. ICMM Rochester New York USA, 2003.

[6] Kandlikar, Satish G. "A roadmap for implementing minichannels in refrigeration and air-conditioning systems—Current status and future directions." *Heat Transfer Engineering* 28.12 (2007): 973-985.

[7] Kandlikar, S. G., and Grande, W. M., Evolution of Microchannel Flow Passages—Thermohydraulic Performance and Fabrication Technology, Heat Transfer Engineering, vol. 24, no. 1, pp. 3–17,2003.

[8] S. Bottillo, A. D. L. Vollaro, G. Galli, and A. Vallati, "ScienceDirect Fluid dynamic and heat transfer parameters in an urban canyon," *Sol. Energy*, vol. 99, pp. 1–10, 2014, doi: 10.1016/j.solener.2013.10.031.

[9] Computational resources provided by hpc@polito, which is a project of Academic Computing within the Department of Control and Computer Engineering at the Politecnico di Torino (http://www.hpc.polito.it)

[10] https://www.plm.automation.siemens.com/global/en/products/simcenter/STAR-CCM.html

[11] https://www.autodesk.com/solutions/cad

[12] https://www.solidworks.com/domain/design-engineering

[13] https://www.mathworks.com/products/matlab/data-analysis.html

[14] Savoldi, Laura, et al. "CFD analysis of different cooling options for a gyrotron cavity." *IEEE Transactions on Plasma Science* 44.12 (2016): 3432-3438.

[15] Bertinetti, Andrea, et al. "Design, test and analysis of a gyrotron cavity mock-up cooled using mini channels." *IEEE Transactions on Plasma Science* 46.6 (2018): 2207-2215.

[16] Allio, Andrea, et al. "Test and modeling of the hydraulic performance of high-efficiency cooling configurations for gyrotron resonance cavities." *Energies* 13.5 (2020): 1163.

[17] S. Stanculovic *et al.*, "Calibration of the KIT test setup for the cooling tests of a gyrotron cavity full-size mock-up equipped with mini-channels," *Fusion Eng. Des.*, vol. 172, p. 112744, Nov. 2021.

[18] https://www.thalesgroup.com/en

[19] Siemens PLM Software Inc, "Star-CCM+ User's Guide v. 15.02." Plano, TX, USA, 2020.

[20] R. Difonzo, A. Allio, and L. Savoldi, "Multivariate metric assessment of the suitability of different RANS turbulence models for the simulation of mini-channels cooling systems for the fusion gyrotron resonator," presented at the ASME V&VUQ symposium 2021.

[21] http://www-ferp.ucsd.edu/LIB/PROPS/PANOS/cu.html

[22] ASM Handbook Committee, p 468-481. DOI: 10.1361/asmhba0005240